

PAPER • OPEN ACCESS

Measurement of the electric permittivity using Bleustein–Gulyaev wave sensor

To cite this article: Alaa Elhady and Eihab Abdel-Rahman 2022 *J. Micromech. Microeng.* **32** 034004

View the [article online](#) for updates and enhancements.

You may also like

- [Temperature hysteresis in the unstable combustion mode of SHS: experiment with high-speed micro-pyrometry](#)
P Gulyaev
- [Acoustoelectronics \(historical review\)](#)
Yurii V Gulyaev
- [High-speed visualization of combustion synthesis discrete reaction waves: coherent heat microstructures](#)
M Boronenko, P Gulyaev and A Dolmatov

Measurement of the electric permittivity using Bleustein–Gulyaev wave sensor

Alaa Elhady*  and Eihab Abdel-Rahman 

Department of System Design Engineering, University of Waterloo, Waterloo N2L 3G1, Ontario, Canada

E-mail: alaaeldin.ahmed@uwaterloo.ca

Received 30 September 2021, revised 10 January 2022

Accepted for publication 24 January 2022

Published 7 February 2022



CrossMark

Abstract

We present a novel compact electric permittivity sensor that exploits Bleustein–Gulyaev waves propagating along the surface of shear-poled piezoelectrics. We formulate the dynamic nonlinear electromechanical partial differential equations of motion governing wave propagation under electromagnetically quasistatic conditions. The permittivity of the medium-under-test was found to influence the sensor eigenvalues, enabling the implementation of a frequency-shift permittivity sensor. Solution of the equations of motion demonstrates resonance of the first and third modes when excited using an interdigitated transducer. We fabricated two sensor prototypes on shear-poled PZT4 and LiNbO₃ substrates and used a Vector Network Analyzer to observe the shift in their fundamental natural frequency in the presence of various media-under-test. S_{11} measurements show deterministic and repeatable shifts in the resonant frequency of the first mode of the LiNbO₃ sensor measured at $\Delta f_1 = 3.51$ MHz for ethanol and $\Delta f_1 = 7.49$ MHz for deionized water where the bare surface frequency was initially at $f_1 = 25.27$ MHz.

Keywords: Bleustein–Gulyaev waves, permittivity sensors, electrostriction, nonlinear dynamics

(Some figures may appear in colour only in the online journal)

1. Introduction

Permittivity sensors identify the dielectric constant, or relative permittivity, of a medium-under-test, and they span over a wide range of applications. Environmental applications include water salinity testing [1, 2] and soil moisture measurement [3]. Such sensors also have industrial applications such as oil characterization [4, 5]. Moreover, they have numerous biological applications, including blood plasma analysis [6, 7], blood alcohol identification [7, 8], and non-invasive glucose detection [9]. It can also be used in DNA-to-RNA differentiation [10], tissue type discrimination [8], cancer cell recognition [11, 12], and viral pathogen detection [13, 14].

Current implementations of permittivity sensors typically operate in the GHz range to limit sensor size, usually on the order of magnitude of the electromagnetic wavelength.

Working in the radio-frequency (RF) range introduces additional complexity to the sensor, such as the need for specialized RF circuits and other design challenges that impact the cost, reliability, and overall device size.

The trade-off between frequency and size creates limits on design flexibility. Decreasing the frequency can enlarge the size to few tens of centimeters [15]. While static (non-resonant) permittivity sensors are not constrained by size, they are dominated by parasitics and thus suffer from low sensitivity [16, 17].

The relationship between the size and operating frequency of resonant permittivity sensors available in the literature is shown in figure 1. The figure illustrates how current technology typically operates in the GHz range and is predominantly in the millimeter to centimeter scale. Only two groups have managed to cross the 1 mm barrier using metamaterials and THz operating frequencies [38, 39].

We propose a novel compact electric permittivity sensor based on Bleustein–Gulyaev waves (BG waves). BG waves

* Author to whom any correspondence should be addressed.



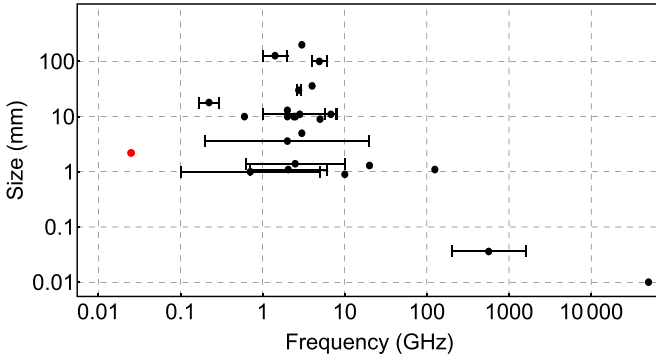


Figure 1. The size vs. operating frequencies of permittivity sensors available in the literature [3, 15, 18–39], References are ordered in descending size. The red marker indicates the LiNbO₃ sensor presented in this work.

were discovered independently by Bleustein [40] and Gulyaev [41]. Since then, they have been under research for their unique nature; coupled electromagnetic and mechanical components that propagate together. The surface shear wave is coupled to a transverse magnetic, TM, electromagnetic field on the surface of shear poled piezoelectrics.

BG waves have several applications, such as liquid property sensing and radio frequency filters. They are attractive for liquid sensing as they are shear waves and do not radiate acoustic energy into the liquid bulk and thus, they avoid micro-streaming effects and realize a high-quality factor. The viscosity and density of the liquid slow down the wave propagation speed and thus create a detectable phase difference with respect to a reference wave [42–46]. Additionally, BG waves have also been shown to work as gyroscopes [47, 48].

BG wave RF filters utilize resonant standing modes to create spectral selectivity. They are more compact than regular Surface Acoustic Wave (SAW) filters [49, 50] since they reflect completely at the edges of the piezoelectric material, eliminating the need for the cascaded electrodes that typical SAW filters use to reflect waves [51]. These filters can operate up to frequencies of 190 MHz and with a low insertion loss [52], thereby exhibiting a high quality factor [50].

We propose to exploit the acoustic speed of BG waves to develop a permittivity sensor that detects disturbances to the electromagnetic field at lengths comparable to the short wavelength of BG waves. As a result, the sensor operating frequency and size can be simultaneously reduced by several orders of magnitude to tens of MHz and few hundred micrometers, respectively.

BG waves exhibit close coupling between electromagnetic and acoustic phenomena. This allows them to serve as sensitive probes for electromagnetic field properties such as the permittivity of a medium-under-test. In this work, we solve the dynamic nonlinear partial differential equations governing the resonant BG waves using the Galerkin Residuals method. We solve the eigenvalue problem to demonstrate the operation of our frequency-shift resonant permittivity sensor. We present simulation results for using a Navy Type II Lead Zirconate Titanate (PZT4) and a Lithium Niobate (LiNbO₃)

piezoelectric substrate. Both materials have been shown to express excellent shear piezoelectric properties and successful history of BG wave implementation [53–56]. Finally, we present experimental validation of the permittivity sensor using the LiNbO₃ substrate.

2. Governing equations

BG waves are comprised of a displacement field $\mathbf{u}(x, y, t)$ coupled to a TM electromagnetic field $\{\mathbf{E}(x, y, t), \mathbf{H}(x, y, t)\}$ [40, 41], such that:

$$\mathbf{u}(x, y, t) = \begin{pmatrix} 0 \\ 0 \\ u_z \end{pmatrix}, \quad \mathbf{E}(x, y, t) = \begin{pmatrix} E_x \\ E_y \\ 0 \end{pmatrix}, \quad \mathbf{H}(x, y, t) = \begin{pmatrix} 0 \\ 0 \\ H_z \end{pmatrix}. \quad (1)$$

BG waves propagate along the x -direction, figure 2(a), on the surface of a piezoelectric substrate, shear-poled in the z -direction. To realize a BG resonator, the wave is excited via a set of interdigitated transducer (IDT) electrodes, figure 2(b), and trapped by two trenches etched at both ends of the resonator, $x=0$ and $x=l$, to reflect the wave [50]. In a resonant sensor, the resonator occupies the lower-half space ($y \geq 0$) while the medium-under-test occupies the upper half-space ($y < 0$).

The stress and polarization tensors reduce to the non-trivial components [57, 58]:

$$T_{yz} = G \frac{\partial u_z}{\partial y} - eE_y - GME_x^2 + GME_y^2 \quad (2)$$

$$T_{xz} = G \frac{\partial u_z}{\partial x} - eE_x - 2GME_xE_y \quad (3)$$

$$D_x = \varepsilon E_x + e \frac{\partial u_z}{\partial x} + 2ME_xT_{yz} + 4ME_yT_{xz} \quad (4)$$

$$D_y = \varepsilon E_y + e \frac{\partial u_z}{\partial y} + 4ME_xT_{xz} - 2ME_yT_{yz} \quad (5)$$

where G is the shear modulus, ε is the zero-strain permittivity of the piezoelectric, $M = M_{14}$ is the electrostrictive constant in the poling direction, and $e = Gd_{15}$ is the zero-strain piezoelectric constant. The governing field equations inside the piezoelectric substrate are the mechanical equation of motion and the relevant Maxwell's equations:

$$\rho \ddot{u}_z + c \dot{u}_z = \frac{\partial T_{xz}}{\partial x} + \frac{\partial T_{yz}}{\partial y} \quad (6)$$

$$\nabla \cdot \mathbf{D} = \zeta - \sigma \int \nabla \cdot \mathbf{E} dt \quad (7)$$

$$\nabla \times \mathbf{E} = -\mu \dot{\mathbf{H}} \quad (8)$$

where ρ is the density of the piezoelectric substrate, c is the viscous damping coefficient, and $\zeta(x, y, t)$ is the charge density distribution. This free charges term is typically ignored in

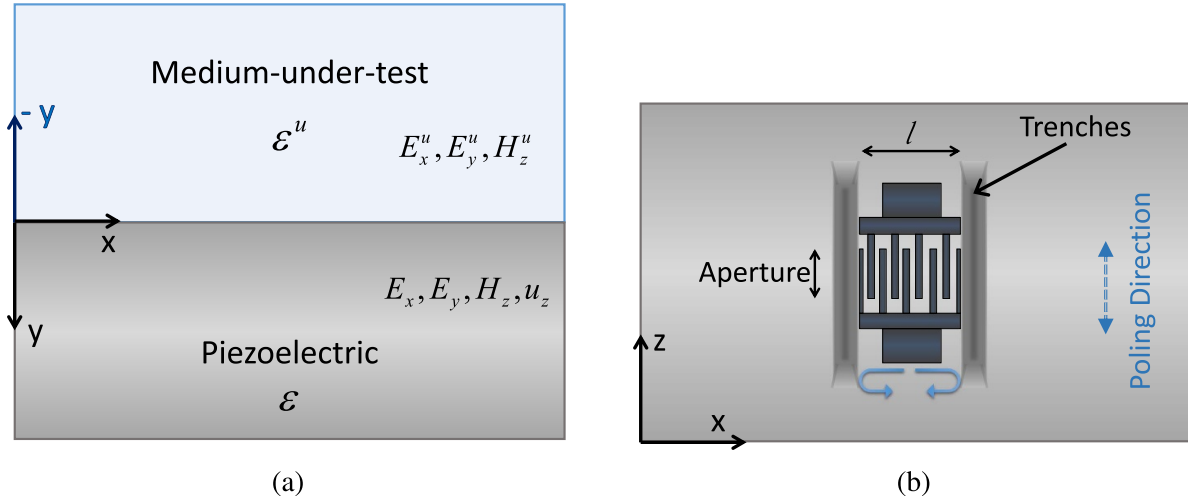


Figure 2. Sensor schematic showing (a) a section view and (b) a top view of the substrate, medium-under-test, and the IDT.

the analysis of SAW. However, this assumption is not valid in this case due to the presence of the IDT on the substrate surface and its function in exciting BG waves. Substituting with equations (2)–(5) into equations (6)–(8), we obtain the governing system of equations [58]:

$$\rho \ddot{u}_z + c \dot{u}_z = G \nabla^2 u_z - e \nabla \cdot \mathbf{E} + ML_1(E_x, E_y) \quad (9)$$

$$\zeta - \sigma \int \nabla \cdot \mathbf{E} dt = e \nabla^2 u_z + \varepsilon \nabla \cdot \mathbf{E} + ML_2(u_z, E_x, E_y) \quad (10)$$

$$\mu \dot{H}_z = \frac{\partial E_x}{\partial y} - \frac{\partial E_y}{\partial x} \quad (11)$$

where $L_1(E_x, E_y)$ and $L_2(u_z, E_x, E_y)$ are the nonlinear electrostriction differential operators, given by equations (53) and (54).

2.1. Boundary conditions and the eigenvalue problem

The resonant sensor is bound by air-filled trenches at the edges. This creates a discontinuity in acoustic impedance and acts as a wave reflector, thereby creating standing waves at resonance. The trenches present as free-end boundary conditions to the acoustic wave.

$$\frac{\partial u_z}{\partial x} \Big|_{x=0} = 0, \quad \frac{\partial u_z}{\partial x} \Big|_{x=l} = 0. \quad (12)$$

Moreover, the surface wave decays exponentially into the substrate [40, 41]:

$$u_z \Big|_{y=\infty} = 0, \quad H_z \Big|_{y=\infty} = 0, \quad (13)$$

$$E_x \Big|_{y=\infty} = 0, \quad E_y \Big|_{y=\infty} = 0. \quad (14)$$

Two matching boundary conditions are imposed at the interface surface ($y = 0$) between the piezoelectric substrate and

the medium-under-test. Assuming that the acoustic pressure applied by the medium-under-test is negligible and ignoring the nonlinear terms, we set the shear stress component T_{yz} to vanish at the surface by requiring that:

$$\frac{\partial u_z}{\partial y} \Big|_{y=0} - \frac{e}{G} E_y \Big|_{y=0} = 0. \quad (15)$$

The second matching condition guarantees the continuity of the electromagnetic field. Dropping the nonlinear terms, this set of boundary conditions can be written as:

$$E_x \Big|_{y=0} - E_x^u \Big|_{y=0} = 0 \quad (16)$$

$$H_z \Big|_{y=0} - H_z^u \Big|_{y=0} = 0 \quad (17)$$

$$D_y \Big|_{y=0} - D_y^u \Big|_{y=0} = 0 \quad (18)$$

where the superscript u denotes the fields in the upper half-space, as shown in figure 2, and $D_y^u = \varepsilon^u E_y^u$.

Therefore the unforced linear eigenfunctions ϕ_n (mode shapes) and eigenvalues ω_n (natural frequencies) can be written as [58]:

$$\phi_n(x, y) = A e^{-\kappa_n y} \cos(k_n x) \quad (19)$$

$$\omega_n = k_n c_s \sqrt{1 - \zeta^2}, \quad k_n = \frac{nm}{l} \pi, \quad \kappa_n = \zeta k_n \quad (20)$$

where n is the mode number, m is the number of IDT fingers, l is the length of the sensor along the propagation direction,

$$c_s = \sqrt{\left(G + \frac{e^2}{\varepsilon}\right) / \rho}$$

is the speed of sound in the substrate, and

$$\zeta = \frac{e^2}{G\varepsilon + e^2} \frac{1}{1 + \frac{\varepsilon^u}{\varepsilon}}$$

is an electromechanical coupling coefficient. To normalized the mode shapes such that:

$$\int_0^\infty \int_0^l \phi_n^2(x, y) dx dy = 1$$

the amplitude is set to: $A = \sqrt{\kappa_n/l}$.

As shown in equation (20), the eigenvalues depend on the permittivity of the medium-under-test ε^u . Therefore, the BG wave resonator can be used as a permittivity sensor by relating ε^u to the measured frequency shift $\Delta\omega_n$. The sensitivity of this sensor can be derived as [59]:

$$S_n = \frac{\partial\omega_n}{\partial\varepsilon^u} = -n \frac{m\pi e^4 r^2}{l(1+r)^2 \sqrt{\rho\varepsilon^3} \sqrt{(1+r)^2(e^2 + G\varepsilon)^3 - e^4(e^2 + G\varepsilon)}} \quad (21)$$

where $r = \frac{\varepsilon^u}{\varepsilon}$ is the ratio of the permittivity of the medium-under-test to that of the piezoelectric substrate.

The partial metallization imposed by the IDT on the surface affects the penetration depth of the BG wave. Therefore, the ratio r representing the electric matching at the surface boundary conditions is modulated by the metalization ratio of the surface by a constant ι . Therefore we redefine the ratio r as:

$$r = \frac{\varepsilon}{\iota\varepsilon^u}.$$

The constant ι can be identified by estimating the penetration depth of the BG wave using a Laser Doppler Vibrometer [60] and was experimentally identified as $\iota = 11.4$. For the case of a metalization ratio of 50%, this is a reasonable value that is close to the literature [50], and the value is applied in further numerical analysis.

2.2. Quasistatic approximation

The propagation speed of BG waves ω_n/k_n , on the order of acoustic speeds, which is much slower than that of electromagnetic waves, at the order of the speed of light. Therefore, variations in the electromagnetic field components appear to occur instantaneously to the elastic field and the governing equations can be further simplified under a quasi-static approximation. Under this assumption, equation (11) can be satisfied by a potential function Ψ , such as:

$$\frac{\partial E_y}{\partial x} - \frac{\partial E_x}{\partial y} = 0 \Rightarrow E_x = -\frac{\partial\Psi}{\partial x}, \quad E_y = -\frac{\partial\Psi}{\partial y} \quad (22)$$

while equations (9) and (10) can, thus, be rewritten as:

$$\rho\ddot{u}_z + c\dot{u}_z = G\nabla^2 u_z + e\nabla^2\Psi + MGL_1(\Psi) \quad (23)$$

$$\zeta + \sigma \int \nabla^2\Psi dt = e\nabla^2 u_z - \varepsilon\nabla^2\Psi + ML_2(u_z, \Psi) \quad (24)$$

where the quasistatic electrostriction differential operators $L_1(\Psi)$ and $L_2(\Psi)$ are given by equations (55) and (56), respectively.

3. Linear BG resonator

We initially investigate the linear resonator response to illustrate the basic operations of the sensor. Dropping the nonlinear terms from equations (23) and (24), we obtained the linear equations of motion:

$$\rho\ddot{u}_z + c\dot{u}_z = G\nabla^2 u_z + e\nabla^2\Psi \quad (25)$$

$$\zeta + \sigma \int \nabla^2\Psi dt = e\nabla^2 u_z - \varepsilon\nabla^2\Psi. \quad (26)$$

Multiplying the second of equations (25) and (26) by e/ε and adding them, we can rewrite the equation of motion as:

$$\rho\ddot{u}_z + \bar{c}\dot{u}_z - \left(G + \frac{e^2}{\varepsilon}\right)\nabla^2 u_z = -\frac{e}{\varepsilon}\zeta \quad (27)$$

where the electric and mechanical energy losses have been lumped into the viscous damping coefficient \bar{c} . This is the equation of a simple harmonic oscillator.

The IDT excites the n th mode of the BG resonator ϕ_n by applying the time-varying voltage distribution

$$V(x, y, t) = V_o e^{-\kappa_n y} \cos(k_n x) \cos(\Omega t) \quad (28)$$

across its fingers, where Ω is the excitation frequency. This voltage will create a charge density distribution, such as:

$$\begin{aligned} \zeta(x, y, t) &= \varepsilon_T \nabla^2 V(x, y, t) \\ &= \varepsilon_T \beta_n^2 V(x, y, t) \end{aligned} \quad (29)$$

where $\beta_n = k_n^2 - \kappa_n^2$. The displacement field can be assumed to a harmonic form of equation (19):

$$u_z(x, y, t) = u(t) e^{-\kappa_n y} \cos(k_n x). \quad (30)$$

Substituting with equations (29) and (30) into equation (27) yields:

$$\ddot{u} + \frac{\omega_n}{Q}\dot{u} + \omega_n^2 u = \frac{f_o}{\rho} \cos(\Omega t) \quad (31)$$

where $\omega_n = \beta_n \sqrt{\frac{G+e^2/\varepsilon}{\rho}}$ is the natural frequency, $Q = \frac{\rho\omega_n}{\bar{c}}$ is the quality factor, and

$$f_o = \frac{e\varepsilon_T}{\varepsilon} \beta_n^2 V_o = \frac{e\omega_n^2}{G} V_o \quad (32)$$

is the forcing amplitude.

For an under-damped system ($Q > \frac{1}{2}$), the displacement field can be written as [61]:

$$u_z(x, y, t) = \frac{\frac{e}{G} V_o}{\sqrt{\left(1 - \frac{\Omega^2}{\omega_n^2}\right)^2 + \left(\frac{\Omega}{\omega_n Q}\right)^2}} e^{-\kappa_n y} \cos(k_n x) \cos(\Omega t). \quad (33)$$

4. Nonlinear BG resonator

4.1. Nondimensional equations of motion

To better capture the detailed dynamic response and exploit it to enhance the sensor sensitivity, we retain the electrostrictive nonlinearity in the equations of motion and account explicitly for the electric damping (dielectric loss). The quasi-static approximation of the nonlinear forced and damped system of equations (23) and (24) is an index-1 system of differential-algebraic equations (DAEs). In fact, this is a nontraditional DAE form due to the integral term on the left-hand side. We reduce the system to an index-0 differential system by differentiating equation (24) once with respect to time, thereby disbanding with the integral term to obtain:

$$\rho \ddot{u}_z + c \dot{u}_z - G \nabla^2 u_z - e \nabla^2 \Psi - MGL_1(\Psi) = 0 \quad (34)$$

$$\dot{\zeta} - e \nabla^2 \dot{u}_z + \varepsilon \nabla^2 \dot{\Psi} + \sigma \nabla^2 \Psi - \hat{M}L_2(u_z, \Psi) = 0. \quad (35)$$

This system is nondimensionalized using the nondimensional variables:

$$\begin{aligned} \hat{x} &= \frac{x}{l}, & \hat{y} &= \frac{y}{l}, & \hat{t} &= \frac{c_s t}{\lambda} \\ \hat{u}_z &= \frac{u_z}{u_o}, & \hat{\Psi} &= \frac{\Psi}{\Psi_o}, & \hat{\zeta} &= \zeta \frac{l^2}{\varepsilon_T \Psi_o} \end{aligned}$$

where $u_o = \frac{e}{G} \Psi_o$ and $\Psi_o = 1$ V. Therefore equations (34) and (35) can be written as:

$$\Lambda_A \triangleq \alpha \ddot{\hat{u}}_z + \hat{c} \dot{\hat{u}}_z - \nabla^2 \hat{u}_z - \nabla^2 \hat{\Psi} - \hat{M}L_1(\hat{\Psi}) = 0 \quad (36)$$

$$\begin{aligned} \Lambda_B \triangleq & \left(1 + \frac{G\varepsilon}{e^2}\right) \dot{\hat{\zeta}} - \nabla^2 \dot{\hat{u}}_z + \frac{G\varepsilon}{e^2} \nabla^2 \dot{\hat{\Psi}} + \frac{G\varepsilon}{e^2} \chi \nabla^2 \hat{\Psi} \\ & - \hat{M}L_2(\hat{u}_z, \hat{\Psi}) = 0 \end{aligned} \quad (37)$$

where:

$$\alpha = \frac{l^2}{\lambda^2} \left(1 + \frac{e^2}{G\varepsilon}\right), \quad \hat{c} = c \sqrt{\frac{\alpha}{\rho G}} l, \quad \hat{M} = \frac{MG}{el}, \quad \chi = \frac{\lambda}{c_s} \sigma.$$

\hat{L}_1 and \hat{L}_2 are nondimensional versions of the differential operators L_1 and L_2 and Λ_A and Λ_B are operators that encase the left-hand sides of the nondimensional system of equations. The hats are henceforth dropped for convenience.

4.2. Discretization

The system is discretized using the Galerkin residuals method [62]. Under the proportional damping assumption, modes that are not directly or indirectly excited vanish over a long-time, leaving directly and indirectly excited modes to carry the energy in the system. Therefore, the Galerkin residuals method can capture most of the energy in the system provided that enough modes are taken in the expansion. Toward that end, the displacement and electric fields are rewritten in terms of

static and dynamic components denoted by the superscripts s and d , respectively, as:

$$u_z(x, y, t) = u_z^s(x, y) + u_z^d(x, y, t) \quad (38)$$

$$\Psi(x, y, t) = \Psi^s(x, y) + \Psi^d(x, y, t). \quad (39)$$

Based on the convergence analysis carried out in [58], the number of modes was set to $N = 4$.

For a four-mode expansion, the static equilibrium can be written as

$$u_z^s(x, y) = \sum_{n=1}^4 q_{sn} \phi_n(x, y) \quad (40)$$

$$\Psi^s(x, y) = \sum_{n=1}^4 p_{sn} \phi_n(x, y) \quad (41)$$

where q_{sn} and p_{sn} are the static modal coordinates. Setting the time derivatives in equation (23) equal to zero, substituting with this form in equations (23) and (24), multiplying the result with each of the mode shapes, and integrating over the domain we obtain a set of algebraic equations (59)–(66) describing the static equilibrium [58]. We note that the electric damping in equation (24) will vanish as described in section 6. Solving this system of equations for q_{sn} and p_{sn} and substituting the result into equations (40) and (41) we obtain the static displacement and potential fields $u_z^s(x, y)$ and $\Psi^s(x, y)$.

Likewise, the dynamic components of the displacement and electric potential are discretized as:

$$u_z^d(x, y, t) = \sum_{n=1}^4 q_n(t) \phi_n(x, y) \quad (42)$$

$$\Psi^d(x, y, t) = \sum_{n=1}^4 p_n(t) \phi_n(x, y) \quad (43)$$

where $q(t)$ and $p(t)$ are time-dependent modal coordinates. The discretized dynamic fields are substituted in the system of equations (36) and (37). The result is multiplied by the mode shapes and integrated over the domain to obtain the residuals as:

$$R_{1n} = \int_0^\infty \int_0^l \phi_n(x, y) \Lambda_A(q_n, p_n) dx dy \quad (44)$$

$$R_{2n} = \partial_t \int_0^\infty \int_0^l \phi_n(x, y) \Lambda_B(q_n, p_n) dx dy \quad (45)$$

where ∂_t denotes the time derivative and $n = 1-4$. The differentiation is carried out first in equation (45) in order to reduce the complexity of the integration. The integration process was carried out symbolically in Mathematica [63]. Setting the residuals R_{1n} and R_{2n} to vanish yields the discretized system of ordinary differential equations, (67)–(74).

Table 1. Specification of the permittivity sensor prototypes.

Substrate material	λ (μm)	Aperture (μm)	Resonance freq. (MHz)
PZT4 [64]	40	400	64.8
LiNbO ₃ [65]	220	2000	21.4

Table 2. Material properties of the sensor substrates.

Property	PZT4 [64, 66]	LiNbO ₃ [65, 67]
G (GPa)	25.6	59.5
e ($\text{N}(\text{V m})^{-1}$)	12.7	4.1
$\varepsilon \times 8.85 \times 10^{-12}$ (F m^{-1})	718	44
ρ (kg m^{-3})	7600	4647

5. Sensor design and fabrication

To test the operation of the permittivity sensor, two prototypes were fabricated using LiNbO₃ and PZT4 polished shear-poled substrates. The distance between the limiting trenches on either side of the IDT and the IDT fingers's periodicity, figure 2(b), were designed to realize the first natural frequencies of the LiNbO₃ and PZT4 sensor prototypes at $f_1 = 21.4$ MHz, and $f_1 = 64.8$ MHz, respectively. The number of IDT fingers was set to $m = 20$ in both cases. The specifications of the prototypes are listed in table 1.

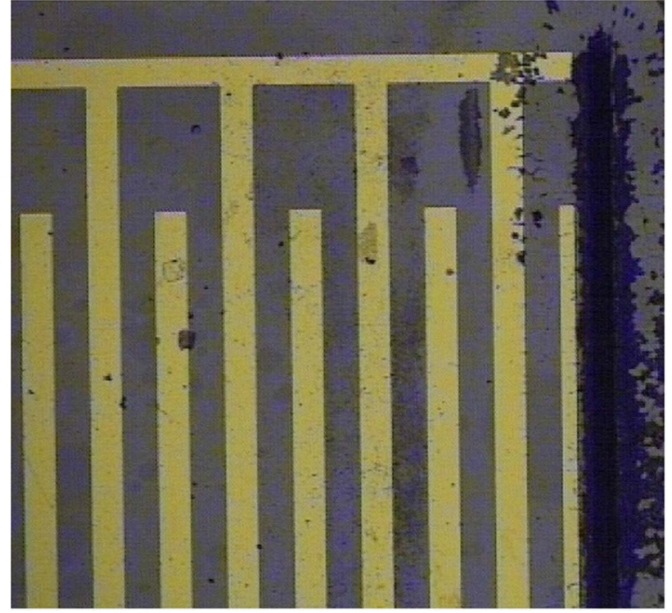
The linear material constants, as specified by the manufacturers and confirmed by comparison to the literature, are listed in table 2. The electrostrictive constants of PZT4 and LiNbO₃ were identified by matching the model predictions to the experimentally measured out-of-plane displacement and found to be $M = 12.7 \times 10^{-18} \text{ m}^2 \text{ V}^{-2}$ and $1.3 \times 10^{-20} \text{ m}^2 \text{ V}^{-2}$ [58].

The IDT was realized on the PZT4 substrate by sputtering a 550 nm thick layer of aluminum. Positive photoresist Shipley-1811 was spun on the substrate and baked. The IDT was patterned in the photoresist using lithography and developed using MF-319. The exposed aluminum was etched with an etchant. After stripping the photoresist, the trenches defining the resonator edges were etched using a laser trimmer (QuickLaze-50).

The LiNbO₃ sensor, figure 3, was fabricated using the same recipe, except that the substrate was pre-coated with 1.1 μm gold/chromium layer, thus obviating the need for the initial metallization step. Minimal localized heat damage can be observed at the edges of the resonator, figure 3, due to laser trimming. The depth of the trenches for the PZT4 and LiNbO₃ sensors were 96 and 76 μm respectively.

6. Results

The charge distribution ζ imposed by the IDT is the excitation signal driving the sensor. Using a Fourier series expansion of equation (29), it can be approximated as [58]:

**Figure 3.** The fabricated LiNbO₃ sensor prototype.**Table 3.** Coefficients of the empirical fit for the charge distribution [58].

$C_1 = 1.115$	$C_5 = -0.019$
$C_3 = -0.103$	$C_7 = 0.005$

$$\zeta(x, y, t) = \varepsilon_T \beta_n^2 \sum_{n=1}^4 C_{2n-1} e^{-\kappa(2n-1)y} \times \cos\left((2n-1)m \frac{\pi x}{l}\right) (V_{DC} + V_{AC} \cos(\Omega t)) \quad (46)$$

where C_{2n-1} are the empirically fitted constants, listed in table 3, and V_{DC} , V_{AC} , and Ω are the bias, amplitude, and frequency of the signal waveform.

The dependence of the dielectric substrate's conductivity σ on the excitation frequency of the electric field can be represented by Jonscher's power law [68]:

$$\sigma = \sigma_{DC} + \varepsilon \tan \delta \Omega^s \quad (47)$$

where σ_{DC} is the frequency invariant component, $\tan \delta$ is the loss tangent representing electrical dissipation in the piezoelectric substrate, and s is a constant such that $0 \leq s \leq 1$. At room temperature, $s \approx 1$ and it decreases as the temperature increases [68]. As a result, the AC conductivity is much larger than its DC counterpart for excitation frequencies in the MHz range. In this work, we assume the substrate to be a perfect insulator at low frequencies. This imposes a limitation on the validity of the model to good dielectrics however, this is true for most piezoelectrics. Therefore, the DC conductivity is neglected, and the total conductivity is approximated as:

$$\sigma \approx \varepsilon \Omega \tan \delta \quad (48)$$

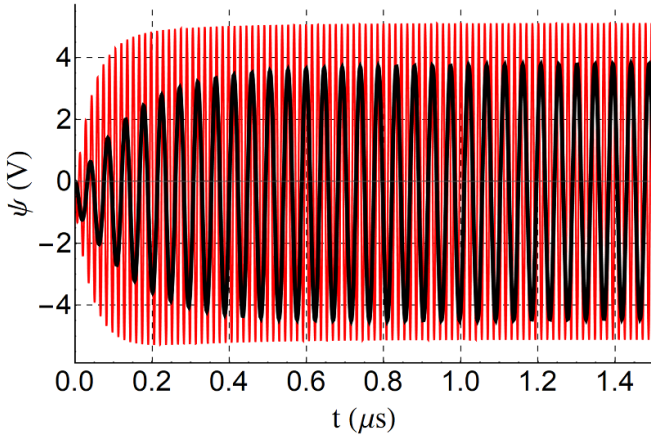


Figure 4. The time evolution of the potential field $\Psi(0,0,t)$ for the PZT4 (red line) and LiNbO₃ (black line) resonators under a pure AC excitation of 1 V_{pp} at the excitation frequencies 64.8 and 21.4 MHz, respectively.

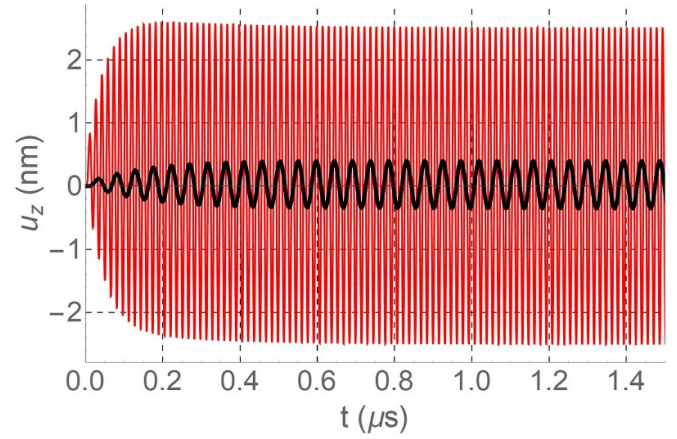


Figure 5. The time evolution of the shear displacement field $u_z(0,0,t)$ for the PZT4 (red line) and LiNbO₃ (black line) resonators under a pure AC excitation of 1 V_{pp} at the frequencies 64.8 and 21.4 MHz, respectively.

where the loss tangent for PZT4 is $\tan\delta = 0.02$ [69] and for LiNbO₃ is $\tan\delta = 0.004$ [70].

The electric forcing and damping terms, equations (46) and (48), as well as the static modal coordinates q_{sn} and p_{sn} are substituted into the system of ordinary differential equations, (67)–(74). The equations are numerically integrated over time for the dynamic modal coordinates $(q_j(t), p_j(t))$, subject to rest initial conditions, and the displacement and potential fields are obtained as:

$$u_z(x,y,t) = \sum_{j=1}^4 (q_{sj} + q_j(t))\phi_j(x,y) \quad (49)$$

$$\Psi(x,y,t) = \sum_{j=1}^4 (p_{sj} + p_j(t))\phi_j(x,y). \quad (50)$$

Figure 4 compares the time evolution of the potential field at the left edge of the PZT4 resonator surface $\Psi(0,0,t)$ to that of the LiNbO₃ resonator. The resonators were excited at their respective natural frequencies, $\Omega = 2\pi \times 64.8$ and $2\pi \times 21.4$ M rad s⁻¹, respectively, with the voltage waveform an $V_{AC} = 0.5$ V and $V_{DC} = 0$ V. In both cases, the mechanical quality factor was set to $Q = 10$, whereas the dielectric loss was set as per equation (48).

Since PZT4 is more conductive than LiNbO₃, it exhibits larger electrical losses and a lower total quality factor than LiNbO₃. As a result, its response, red line in figure 4, has a shorter settling time than that of LiNbO₃ (black line). On the other hand, even though the LiNbO₃ resonator has a higher effective quality factor, its steady-state potential is lower than that of PZT4 due to a lower electromechanical coupling coefficient $\sqrt{e^2/(G\epsilon + e^2)}$ [55]. PZT4 is more efficient in coupling the excitation voltage to the potential field than LiNbO₃, with a coupling coefficient of 70.6% for PZT4 compared to 64.8% for LiNbO₃. The same trends are also evident in comparing the displacement fields, figure 5, of the PZT4 and LiNbO₃ resonators at $u_z(0,0,t)$.

Three different media were tested, namely, air, ethanol, and deionized (DI) water. Although BG waves have been previously used to sense viscosity, they were deployed in a line-delay configuration rather than a resonator. When used in a resonant configuration, the viscosity of the medium-under-test would not affect the natural frequency [43]. However, as a precaution, this was taken into consideration. At room temperature, ethanol and DI water have similar viscosities but different relative permittivities at 24 and 78, respectively [71, 72]. Therefore they present suitable candidates for the characterization of a permittivity sensor.

The frequency-response curves of the displacement and potential fields are shown in figures 6 and 7, respectively, for the PZT4 sensor with air (black), ethanol (red), and DI water (blue) media-under-test. The curves show the peak-to-peak displacement $u_{z(pp)}$ and potential $\Psi_{(pp)}$ at the origin, point (0,0). The frequency sweep was carried out numerically by solving equations (67)–(74) subject to a voltage waveform with a constant amplitude $V_{AC} = 0.5$ V and with the frequency varying in the range $\Omega = 2\pi \times [13, 265]$ M rad s⁻¹. The steady-state response was obtained by carrying long-time integration for 300 excitation periods and recording the peak-to-peak response during the last 10 periods of the time history. The excitation frequency was increased in steps varying in size from 20 kHz, close to resonance, to 500 kHz away from resonances. After each frequency step, the initial conditions were taken as the modal coordinates of the last point in the time-history of the previous excitation frequency.

The response curves show evidence of primary resonance in the vicinity of the first and third modes. This reflects the fact the IDT geometry, described in equation (46), represents direct excitation for both modes. The effective quality factors of the first ($f_1 = 64.8$) and third ($f_3 = 194.4$) modes were calculated from the response curves using the half-power bandwidth method and found to be $Q_1 = 8.5$ and $Q_3 = 27$. It is interesting to note that the potential response curves exhibit evidence of anti-resonance, figure 7, but not those of the displacement field, figure 6, indicating lower electric losses.

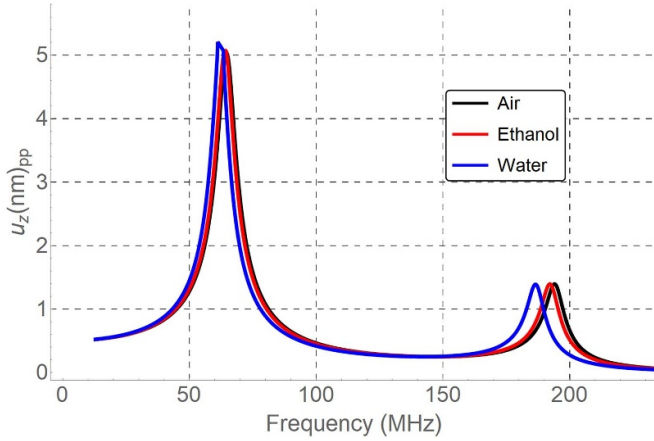


Figure 6. The frequency-response curves of the shear displacement field u_z at the origin $(0, 0)$ of the PZT4 sensor under a voltage waveform with an amplitude of $V_{AC} = 0.5$ V for three media-under-test.

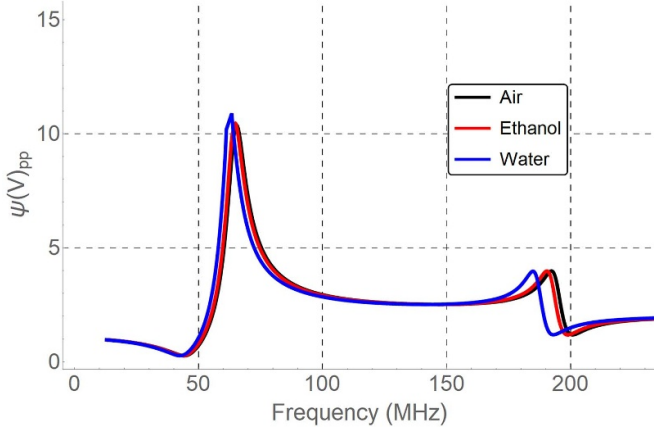


Figure 7. The frequency-response curves of the potential field Ψ at the origin $(0, 0)$ of the PZT4 sensor under a voltage waveform with an amplitude of $V_{AC} = 0.5$ V for three media-under-test.

Both resonant peaks, figures 6 and 7, shift to lower frequencies as the permittivity of the medium-under-test increases. The sensitivity of the third mode toward changes in permittivity is more than that of the lower mode, as evidenced by a larger frequency shift. Specifically, the resonant frequency of the first mode shifts down by $\Delta f_1 = 0.65$ MHz in the presence of ethanol and by $\Delta f_1 = 2.5$ MHz in the presence of water compared to $\Delta f_3 = 1.84$ MHz and $\Delta f_3 = 7.5$ MHz for the third mode. The drop in the resonant frequency with increased medium-under-test permittivity is expected, as per equation (20). Higher permittivity leads to stronger coupling between BG waves and the medium-under-test represented by a larger capacitance of that medium. The elevated sensitivity of the third mode compared to the first mode is also expected since the sensitivity, equation (21), is linearly proportional to mode number n .

The amplitude of the higher mode is less than that of the lower mode because the direct excitation of the IDT to the higher mode is smaller than that of the lower mode, see table 3. Further, higher modes are stiffer, therefore requiring

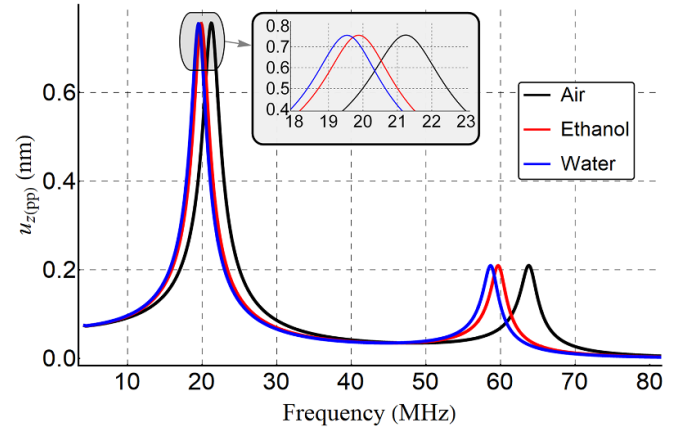


Figure 8. The frequency-response curves of the shear displacement field u_z at the origin $(0, 0)$ of the LiNbO₃ sensor under a voltage waveform with an amplitude of $V_{AC} = 0.5$ V for three media-under-test.

larger forcing to realize similar amplitudes. This presents a trade-off between modal sensitivity and their signal-to-noise ratio (SNR). When the material under test was DI water, the numerical solver broke down over five frequency steps in a small region around the peak of the first mode, figures 6 and 7, due to numerical stiffness.

The frequency-response curves of the LiNbO₃ sensor were obtained numerically using the same procedure and voltage waveforms except that the frequency of excitation was swept in the range $\Omega = 2\pi \times [4, 88]$ M rad s⁻¹ to capture the primary resonance of the first ($f_1 = 21$ MHz) and third ($f_3 = 63$ MHz) modes. The frequency steps varied in size from 6.8 kHz, close to resonance, to 170 kHz away from the resonances. The frequency-response curves of the peak-to-peak displacement $u_{z(pp)}$ and potential $\Psi_{(pp)}$ at the origin $(0, 0)$ are shown in figures 8 and 9, respectively, for air (black), ethanol (red), and DI water (blue) media-under-test. The sensor was designed using a larger wavelength λ specifically in order to reduce its natural frequencies, thereby simplifying the experimental setup.

Similar to the PZT4 sensor, both resonant peaks shift to lower frequencies as the permittivity of the medium-under-test increases. Further, the third mode was also found to be more sensitive than the first mode. Specifically, the resonant frequency of the first mode shifts down by $\Delta f_1 = 1.38$ MHz in the presence of ethanol and by $\Delta f_1 = 1.72$ MHz in the presence of DI water compared to $\Delta f_3 = 4.11$ MHz and $\Delta f_3 = 5.12$ MHz for the third mode.

The ratio of the frequency shift to the first natural frequency in LiNbO₃ sensor is 6.5% for ethanol and 8% for DI water, while for the PZT4 sensor, it is 1% for ethanol and 3.8% for DI water. Therefore, the LiNbO₃ sensor is more sensitive to changes in permittivity than the PZT4 sensor. This is in agreement with the findings in [73], namely that sensitivity improves as the permittivity of the medium-under-test approaches half the permittivity of the sensor substrate. However, this comes at the expense of a smaller SNR and weaker potential and displacement fields for the LiNbO₃

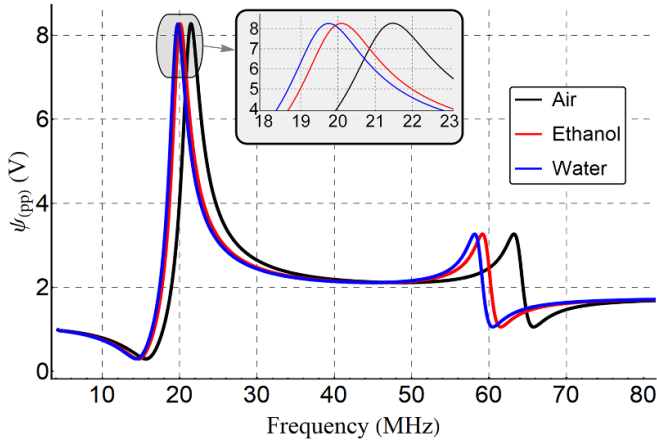


Figure 9. The frequency-response curves of the potential field ψ at the origin $(0, 0)$ of the LiNbO_3 sensor under a voltage waveform with an amplitude of $V_{AC} = 0.5$ V for three media-under-test.

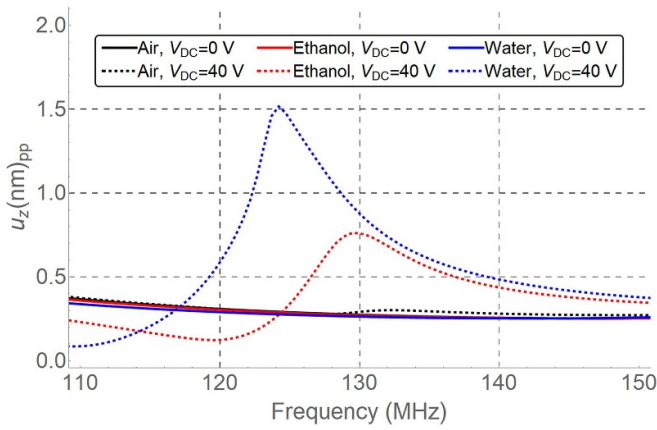


Figure 10. The frequency-response curves of the shear displacement field u_z at the origin $(0, 0)$ of the PZT4 sensor in the vicinity of the second mode natural frequency f_2 for three media-under-test. The sensor is excited with an unbiased voltage waveform (solid lines) and a waveform biased with $V_{DC} = 40$ V (dashed lines). The AC amplitude for both waveforms is $V_{AC} = 0.5$ V.

sensor. Thus, this presents a trade-off between sensitivity and SNR.

To investigate the impact of the electrostrictive nonlinearity, the frequency response of the sensor was evaluated under biased and unbiased voltage waveforms. Figures 10 and 11 show the frequency-response curves of the PZT4 sensor's peak-to-peak displacement $u_{z(pp)}$ and potential $\psi_{(pp)}$ at the origin $(0, 0)$, respectively, in the vicinity of the second mode natural frequency f_2 . Both waveforms had the same AC amplitude $V_{AC} = 0.5$ V, one was unbiased with $V_{DC} = 0$ V, shown in solid lines, and the other was biased with $V_{DC} = 40$ V, shown in dashed lines.

The impact of the quadratic electrostrictive nonlinearity can be clearly seen in the activation of the second mode. While the biased voltage waveform excites the primary resonance of that mode, the unbiased voltage waveform fails to excite it. The resonant peak of the second mode does not only shift to lower

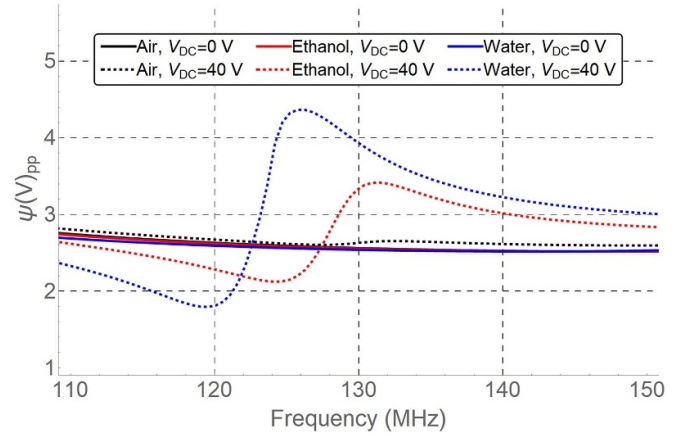


Figure 11. The frequency-response curves of the potential field ψ at the origin $(0, 0)$ of the PZT4 sensor in the vicinity of the second mode natural frequency f_2 for three media-under-test. The sensor is excited with an unbiased voltage waveform (solid lines) and a waveform biased with $V_{DC} = 40$ V (dashed lines). The AC amplitude for both waveforms is $V_{AC} = 0.5$ V.

frequencies, like the first and third modes, but also increases in magnitude as the permittivity of the medium-under-test increases. However, the use of DC voltage with electrolytic test media, such as water, presents a challenge since it will result in electrolysis. This issue will be further investigated in future work.

7. Experimental validation and discussion

7.1. Experimental setup

Figure 12 shows the experimental setup including a vector network analyzer (VNA), Agilent E5061B, and the microscopic positioner of a Laser Doppler Vibrometer, Polytech Inc. MSA-600. The VNA was used to measure the sensors' scattering parameter $S_{11}(f)$ representing the reflection coefficient of the input port at a given excitation frequency. Since the sensors were configured as one-port resonators, S_{11} was enough to fully characterize them. The sensors admit only resonant waves and reflect waves with frequencies away from their natural frequencies. Therefore, resonance appears in S_{11} measurements as a valley.

The power level of the VNA was set to 10 dBm, and the intermediate frequency bandwidth, IF-BW, was set to 30 kHz. Each measurement was averaged ten times. The sensor pads were directly probed under the microscope, figure 12(b), and the probe station was operated by a two-dimensional motorized positioner. Port 1 of the VNA was directly connected to the probe station using a short coaxial cable. The VNA was calibrated to compensate for the probes and cables, source mismatch, probes reflections, and cross-talk.

7.2. S-parameters modeling

The complex scattering parameter S_{11} is a function of the impedance mismatch between the resonator impedance Z_{11}

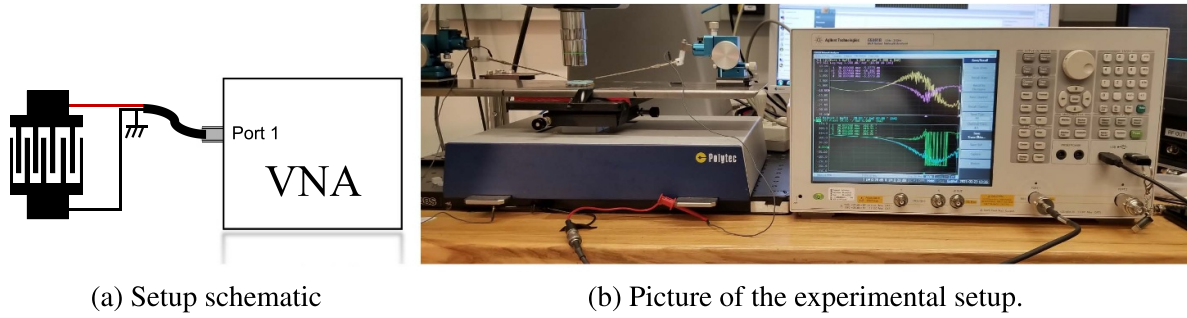


Figure 12. Experimental characterization of the permittivity sensors.

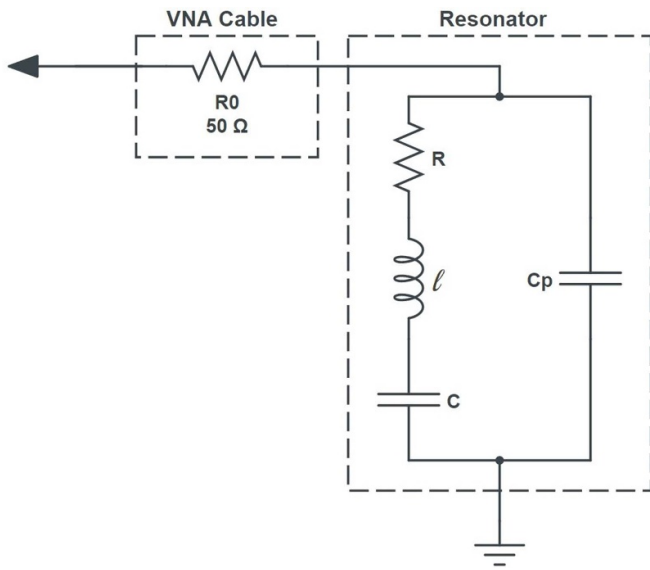


Figure 13. The equivalent circuit for the BG resonator and the VNA cable.

and the cable impedance $Z_o = 50 \Omega$, figure 13. It can be written as [74]:

$$S_{11} = \frac{Z_{11} - Z_o}{Z_{11} + Z_o} \quad (51)$$

The resonator is modeled as a resonant (R-L-C) circuit with resistance, inductance, and capacitance of R , l , and c , coupled to the parasitic capacitance c_p of the IDT, figure 13. Therefore, its impedance can be modeled as:

$$Z_{11} = \frac{X_c Z}{X_c - Z} \quad (52)$$

where $X_c = 1/(i2\pi f c_p)$ and $Z = R + (i2\pi f c)^{-1} + i2\pi f l$ are the parasitic and resonant circuit impedance, respectively. The resonant circuit parameters, R , l , and c , were extracted from the simulated or measured f_1 and Q_1 following the procedure described by Soluch [75].

The circuit in figure 13 is a simplified representation of the resonator used to identify parasitic capacitance c_p encountered in the experimental setup. It was identified by matching the experimentally measured S_{11} to the model predicted S_{11} as

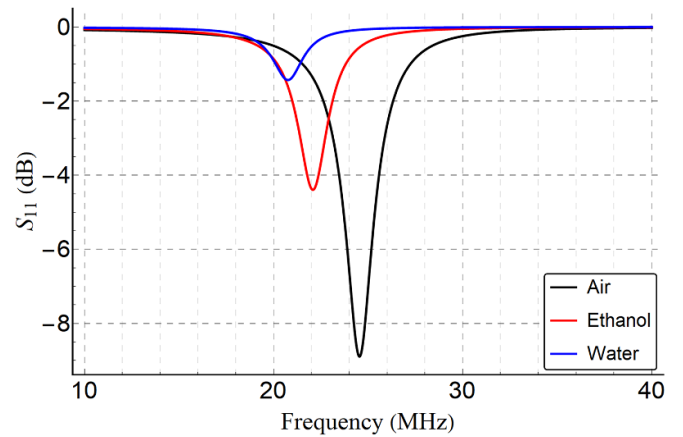


Figure 14. Modeled S-parameters based on the R-L-C model for the LiNbO₃ based sensor, with a parasitic capacitor, for air, ethanol and water, as the medium-under-test.

per equation (51). The identified parasitic capacitance, for the LiNbO₃ sensor, was found to be $c_{p_o} = 794$ pF.

The parasitic capacitance of the IDT is affected by the permittivities of the substrate and the medium-under-test. Since the IDT thickness is small compared to its length, width, and gap, its capacitance is dominated by fringing effects [76] in the upper and lower half-spaces. Therefore, the effective permittivity of the parasitic capacitor can be approximated as the average of those of the piezoelectric and the medium-under-test. The ratio of the parasitic capacitance in the presence of a medium-under-test c_{p_m} to that of the bare surface c_{p_o} can thus be approximated as:

$$\frac{c_{p_m}}{c_{p_o}} = \frac{\epsilon + \epsilon''}{\epsilon + 1}$$

This ratio is thus used to account for the change in the parasitic capacitance of the sensor when used with different media-under-test. Figure 14 shows the modeled S_{11} of the LiNbO₃ sensor as a function of the frequency when used with air, ethanol, and DI water.

7.3. Sensor validation

As described, ethanol and DI water are suitable media for sensor validation. The results of using the VNA to characterize

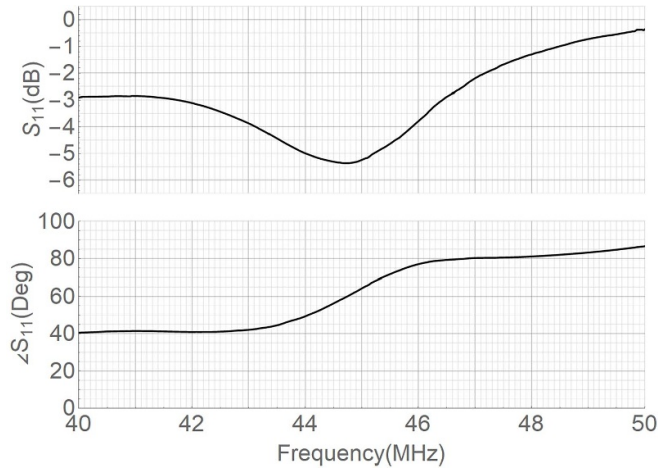


Figure 15. Experimental S_{11} measurements for the PZT4 sensor in air.

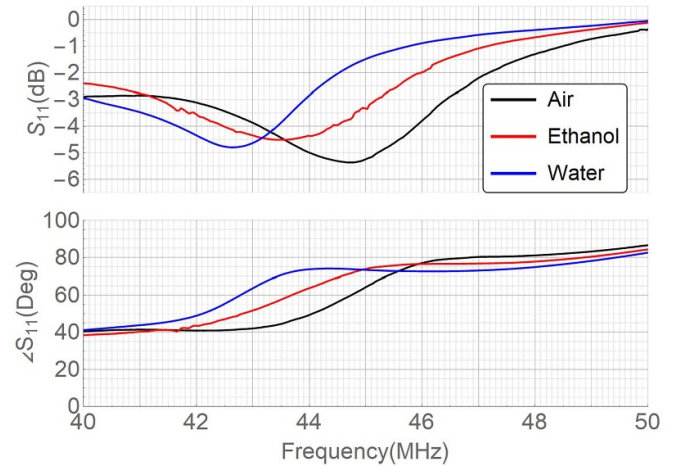


Figure 17. Experimental S_{11} measurements for the PZT4 sensor for different media-under-test.

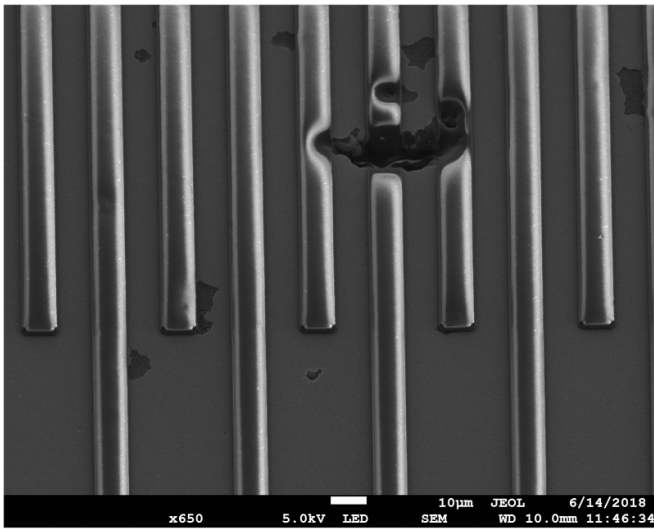


Figure 16. Scanning electron microscopic images of the surface of the PZT4 sensor. The porous nature of PZT4 will degrade the sensor performance.

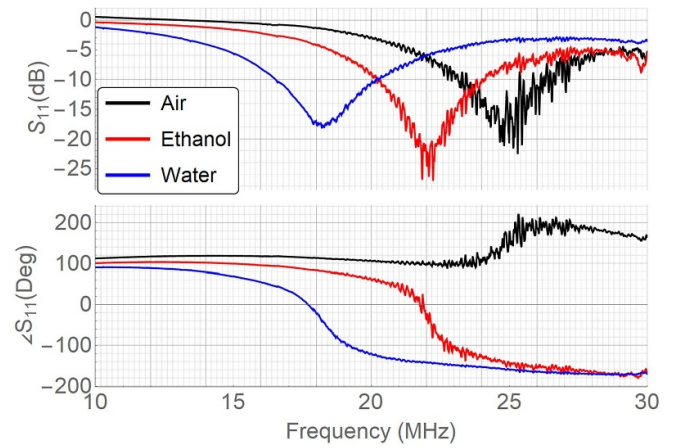


Figure 18. Experimental S_{11} measurements for the $LiNbO_3$ sensor for different media-under-test.

the PZT4 based sensor are shown in figure 15. This PZT4 sensor did not yield promising results and had a low return-loss of 5.5 dB, figure 15. Additionally, the recorded resonance frequency, 44.7 MHz, was lower than the designed value of 64.8 MHz. This deviation can be attributed to uncertainty in the fabricated IDT dimensions as well as surface porosity, and it was found to exist for multiple tested PZT4 based sensors. The surface of the polished PZT4 substrate was found to be porous, figure 16, with pores that are in the order of the sensor’s wavelength.

The S_{11} measurements using the PZT4 sensor with the media-under-test of air (black), ethanol (red), and water (blue) are shown figure 17. However, due to the aforementioned challenges, it was concluded that further testing and analysis of the PZT4 are suspended due to fabrication issues.

On the other hand, the $LiNbO_3$ sensor showed promising results, figure 18. The figure shows the S_{11} vs. frequency with

the medium-under-test set as air (black), ethanol (red), and DI water (blue). The ethanol and DI water samples were deposited using a pipette, figure 19, on the entire surface of the sensor. The return-loss observed for all the tests was well above 15 dB. However, the $LiNbO_3$ sensor exhibits more evidence of noise than the PZT4 sensor because the excitation force applied to it is lower than its PZT4 sensor counterpart due to the larger electromechanical coupling coefficient of PZT4.

The measurements in figure 18 were repeated several times, and the statistical mean and standard deviation were recorded in table 4. The frequency response of using either air or ethanol as the medium-under-test, figure 18 is in good agreement with the modeled S-parameters, figure 14, in terms of the position of the S_{11} minima on the frequency axis. However, the values of the S_{11} minima on the y-axis do not match. Such values depend on two factors, the electrical matching and the damping effect of the viscous loading of liquids on the surface, and they would not interfere with the operation of the frequency-shift sensor.

The realized quality factors are low compared to those in the literature [77, 78] due to the challenges encountered in patterning the trenches. Both the heat damage to the edges of

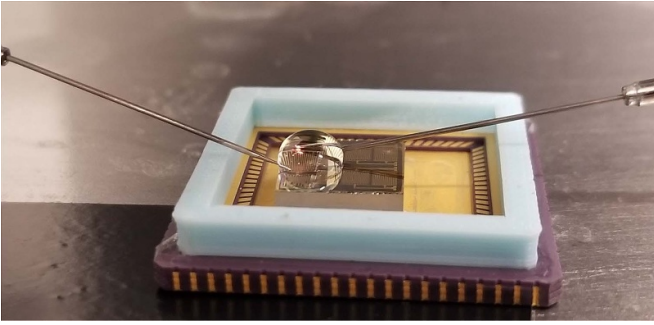


Figure 19. Probing of the LiNbO₃ sensor, with a DI water droplet covering its surface.

Table 4. Statistical results of the experimental measurements for the LiNbO₃ based sensor for different media-under-test.

Medium-under-test	Air	Ethanol	DI water
Mean of f_1 (MHz)	25.27	21.76	17.78
Standard deviation of f_1 (MHz)	0.09	0.48	0.49
Mean quality factor Q_1	11	12	9

Table 5. Comparison of theoretical with experimental natural frequencies (f_1) for the LiNbO₃ sensor under different media-under-test.

Medium-under-test	Air	Ethanol	DI water
Model (MHz)	24.54	22.09	20.73
Experiment (MHz)	25.27	21.76	17.78
Error	2.9%	−1.5%	−16.6%

the resonators and the limited depth of the trenches reduce the edge reflectivity, thus increasing energy losses and reducing the quality factor. Additionally, the number, shape, height, and dimensions of IDT fingers affect the quality factor of the SAW resonators [79–81]. Optimizing them can help reduce energy losses and increase the quality factor.

The error in the position of the S_{11} minima was found to be smaller than 3% when compared with the numerical results, table 5. However, the DI water was found to have an enhanced frequency shift. This shift warrants further investigation in future work. It may have arisen due to contamination resulting in non-zero ionic concentrations or an elevated sample temperature due to dielectric heating.

7.4. Discussion

The results show a clear relation between the permittivity of the medium-under-test and the resonance frequency of the BG wave sensor. Furthermore, the shift due to the permittivity of the medium-under-test from the natural frequency with the sensor in air is not linear. It depends on the sensitivity of the eigenvalue of the BG wave sensor, equation (21), to the ratio of the permittivity of the substrate to that of the medium-under-test, r . Moreover, the electrostrictive nonlinearity in the substrate affects the sensitivity. This could be further exacerbated under DC bias [58].

It is also influenced by several other factors, and they must all be taken into consideration. The effect of the partial metalization imposed by the IDT on the surface, which directly affects the wave confinement to the surface. The confinement degree can be characterized using a Laser Doppler Vibrometer [60], in order to estimate the surface metalization effect.

The parasitic capacitance, which influences electrical measurements, such as S_{11} . The parasitic capacitance acts in parallel to the resonator and must be considered, equation (51), in order to correctly predict the frequency response of the S_{11} parameter. The effect of the media-under-test on the parasitic capacitance enhances the observed sensitivity of the sensor and thus is desirable. However, on its own and without the BGW equations, it is not nearly sufficient to explain the experimentally observed frequency shifts under different media-under-test.

8. Conclusion

We presented a novel permittivity sensor using BG waves. The sensor was modeled and experimentally verified. The non-linear partial differential equations of motion governing the sensor response under electromagnetically quasistatic excitation were solved using the Galerkin residuals method. Eigenvalue analysis indicates that the medium-under-test influences the sensor eigenvalues, enabling the implementation of a frequency-shift permittivity sensor.

The model was used to plot time evolution and the frequency response of the sensors. We find that the first and third modes of primary resonance were directly excited and that higher modes exhibited higher sensitivity to the permittivity of the media-under-test. We also find that under applied DC voltage, the second mode of primary resonance is excited due to the presence of electrostrictive nonlinearities. However, aquatic-based media-under-test presents a challenge, as water tends to experience electrolysis. This is an open research challenge and would need to be further investigated in future work.

Two sensor prototypes were fabricated on PZT4 and LiNbO₃ substrates. The fundamental natural frequencies of bare surface sensors were characterized using a VNA and were found to be $f_1 = 44.7$ MHz and $f_1 = 25.27$ MHz, respectively. The LiNbO₃ sensor exhibited superior performance in terms of return-loss over the PZT4 sensor. Two media-under-test, DI water and ethanol, were used to demonstrate the LiNbO₃ sensor. The first mode's fundamental natural frequency was observed to shift downward in the presence of ethanol by $\Delta f_1 = 3.51$ MHz and in the presence of DI water by $\Delta f_1 = 7.49$ MHz, thereby demonstrating a sensor sensitivity in the range of 100–150 kHz $(F\ m^{-1})^{-1}$.

Data availability statement

The data that support the findings of this study are available upon reasonable request from the authors.

Conflict of interest

The authors declare that they have no conflict of interest.

Appendix

A.1. Electrostriction operators

The electrostriction operators L_1 and L_2 appearing in the wave equations, (9) and (10), are defined as:

$$L_1(E_x, E_y) = G \nabla \cdot \left(\begin{matrix} -2E_x E_y \\ E_y^2 - E_x^2 \end{matrix} \right) \quad (53)$$

$$L_2(u_z, E_x, E_y) = 2 \left(-4eE_x \frac{\partial E_x}{\partial y} - 3eE_x \frac{\partial E_y}{\partial x} - 3eE_y \frac{\partial E_x}{\partial x} + 2eE_y \frac{\partial E_y}{\partial y} + 2G \frac{\partial u_z}{\partial x} \left(\frac{\partial E_x}{\partial y} + \frac{\partial E_y}{\partial x} \right) - G \frac{\partial u_z}{\partial y} \left(\frac{\partial E_y}{\partial y} - \frac{\partial E_x}{\partial x} \right) + 2GE_y \frac{\partial^2 u_z}{\partial x^2} - GE_y \frac{\partial^2 u_z}{\partial y^2} + 3GE_x \frac{\partial^2 u_z}{\partial x \partial y} - 3GM(E_x^2 + E_y^2) \nabla \cdot \left(\begin{matrix} E_x \\ E_y \end{matrix} \right) - 6GME_x E_y \nabla \cdot \left(\begin{matrix} E_y \\ E_x \end{matrix} \right) \right). \quad (54)$$

In potential form, the operators reduce to:

$$L_1(\Psi) = 2 \left(\frac{\partial \Psi}{\partial y} \frac{\partial^2 \Psi}{\partial y^2} - \frac{\partial \Psi}{\partial y} \frac{\partial^2 \Psi}{\partial x^2} - 2 \frac{\partial \Psi}{\partial x} \frac{\partial^2 \Psi}{\partial x \partial y} \right) \quad (55)$$

$$L_2(u_z, \Psi) = eL_{2A}(u_z, \Psi) + MGL_{2B}(u_z, \Psi) \quad (56)$$

$$L_{2A}(u_z, \Psi) = \frac{\partial \Psi}{\partial y} \left(-6 \frac{\partial^2 \Psi}{\partial x^2} + 4 \frac{\partial^2 \Psi}{\partial y^2} - 4 \frac{G}{e} \frac{\partial^2 u_z}{\partial x^2} + 2 \frac{G}{e} \frac{\partial^2 u_z}{\partial y^2} \right) - \frac{\partial \Psi}{\partial x} \left(14 \frac{\partial^2 \Psi}{\partial x \partial y} + 6 \frac{G}{e} \frac{\partial^2 u_z}{\partial x \partial y} \right) + 2 \frac{G}{e} \frac{\partial u_z}{\partial y} \left(\frac{\partial^2 \Psi}{\partial y^2} - \frac{\partial^2 \Psi}{\partial x^2} \right) - 8 \frac{G}{e} \frac{\partial u_z}{\partial x} \frac{\partial^2 \Psi}{\partial x \partial y} \quad (57)$$

$$L_{2B}(u_z, \Psi) = 6 \left(\frac{\partial^2 \Psi}{\partial x^2} + \frac{\partial^2 \Psi}{\partial y^2} \right) \left(\left(\frac{\partial \Psi}{\partial y} \right)^2 + \left(\frac{\partial \Psi}{\partial x} \right)^2 \right) + 24 \frac{\partial \Psi}{\partial x} \frac{\partial \Psi}{\partial y} \frac{\partial^2 \Psi}{\partial x \partial y}. \quad (58)$$

A.2. Equilibrium algebraic equations

The discretized equilibrium equations for a four-mode approximation can be written as [58]:

$$p_{s1} + q_{s1} + \alpha_1 p_{s1} p_{s2} + \alpha_2 p_{s2} p_{s3} + \alpha_3 p_{s3} p_{s4} = 0 \quad (59)$$

$$p_{s2} + q_{s2} + \alpha_4 p_{s1}^2 + \alpha_5 p_{s1} p_{s3} + \alpha_6 p_{s2} p_{s4} = 0 \quad (60)$$

$$p_{s3} + q_{s3} + \alpha_7 p_{s1} p_{s2} + \alpha_8 p_{s1} p_{s4} = 0 \quad (61)$$

$$p_{s4} + q_{s4} + \alpha_9 p_{s2}^2 + \alpha_{10} p_{s1} p_{s3} = 0 \quad (62)$$

$$q_{s1} + \alpha_{11} p_{s1} + \alpha_{12} p_{s1}^3 + \alpha_{29} V_{DC} + \alpha_{13} p_{s1} p_{s2} + \alpha_{14} p_{s1} p_{s2}^2 + \alpha_{15} p_{s1}^2 p_{s3} + \alpha_{16} p_{s2} p_{s3} + \alpha_{17} p_{s2}^2 p_{s3} + \alpha_{18} p_{s1} p_{s3}^2 + \alpha_{20} p_{s3} p_{s4} + \alpha_{22} p_{s1} p_{s4}^2 + \alpha_{23} p_{s2} q_{s1} + \alpha_{24} p_{s1} q_{s2} + \alpha_{25} p_{s3} q_{s2} + \alpha_{26} p_{s2} q_{s3} + \alpha_{27} p_{s4} q_{s3} + \alpha_{28} p_{s3} q_{s4} + \alpha_{19} p_{s1} p_{s2} p_{s4} + \alpha_{21} p_{s2} p_{s3} p_{s4} = 0 \quad (63)$$

$$q_{s2} + \alpha_{30} p_{s1}^2 + \alpha_{11} p_{s2} + \alpha_{32} p_{s2}^3 + \alpha_{31} p_{s1}^2 p_{s2} + \alpha_{33} p_{s1} p_{s3} + \alpha_{35} p_{s2} p_{s3}^2 + \alpha_{36} p_{s1}^2 p_{s4} + \alpha_{37} p_{s2} p_{s4} + \alpha_{39} p_{s3}^2 p_{s4} + \alpha_{40} p_{s2} p_{s4}^2 + \alpha_{41} p_{s1} q_{s1} + \alpha_{42} p_{s3} q_{s1} + \alpha_{43} p_{s4} q_{s2} + \alpha_{44} p_{s1} q_{s3} + \alpha_{45} p_{s2} q_{s4} + \alpha_{34} p_{s1} p_{s2} p_{s3} + \alpha_{38} p_{s1} p_{s3} p_{s4} = 0 \quad (64)$$

$$q_{s3} + \alpha_{46} p_{s1}^3 + \alpha_{11} p_{s3} + \alpha_{51} p_{s3}^3 + \alpha_{59} V_{DC} + \alpha_{47} p_{s1} p_{s2} + \alpha_{48} p_{s1} p_{s2}^2 + \alpha_{49} p_{s1}^2 p_{s3} + \alpha_{50} p_{s2}^2 p_{s3} + \alpha_{52} p_{s1} p_{s4} + \alpha_{55} p_{s3} p_{s4}^2 + \alpha_{56} p_{s2} q_{s1} + \alpha_{57} p_{s4} q_{s1} + \alpha_{56} p_{s1} q_{s2} + \alpha_{58} p_{s1} q_{s4} + \alpha_{53} p_{s1} p_{s2} p_{s4} + \alpha_{54} p_{s2} p_{s3} p_{s4} = 0 \quad (65)$$

$$q_{s4} + \alpha_{61} p_{s2}^2 + \alpha_{11} p_{s4} + \alpha_{68} p_{s4}^3 + \alpha_{60} p_{s1}^2 p_{s2} + \alpha_{62} p_{s1} p_{s3} + \alpha_{64} p_{s2} p_{s3}^2 + \alpha_{65} p_{s1}^2 p_{s4} + \alpha_{66} p_{s2}^2 p_{s4} + \alpha_{67} p_{s3}^2 p_{s4} + \alpha_{69} p_{s3} q_{s1} + \alpha_{70} p_{s2} q_{s2} + \alpha_{69} p_{s1} q_{s3} + \alpha_{63} p_{s1} p_{s2} p_{s3} = 0 \quad (66)$$

where the coefficients α_i depend on the substrate properties and the permittivity ratio r .

A.3. Dynamic ordinary differential equations

The discretized equations of motion for a four-mode approximation can be written as:

$$\ddot{q}_1 + \alpha_{71} p_1 + \alpha_{71} q_1 + \alpha_{75} \dot{q}_1 + \alpha_{72} p_{s2} p_1 + \alpha_{72} p_{s1} p_2 + \alpha_{73} p_{s3} p_2 + \alpha_{72} p_1 p_2 + \alpha_{73} p_{s2} p_3 + \alpha_{74} p_{s4} p_3 + \alpha_{73} p_2 p_3 + \alpha_{74} p_{s3} p_4 + \alpha_{74} p_3 p_4 = 0 \quad (67)$$

$$\ddot{q}_2 + \alpha_{78} p_1^2 + \alpha_{79} p_2 + \alpha_{79} q_2 + \alpha_{75} \dot{q}_2 + \alpha_{76} p_{s1} p_1 + \alpha_{77} p_{s3} p_1 + \alpha_{80} p_{s4} p_2 + \alpha_{77} p_{s1} p_3 + \alpha_{77} p_1 p_3 + \alpha_{80} p_{s2} p_4 + \alpha_{80} p_2 p_4 = 0 \quad (68)$$

$$\ddot{q}_3 + \alpha_{83}p_3 + \alpha_{83}q_3 + \alpha_{75}\dot{q}_3 + \alpha_{82}p_{s4}p_1 + \alpha_{81}p_{s2}p_1 + \alpha_{81}p_{s1}p_2 + \alpha_{81}p_1p_2 + \alpha_{82}p_{s1}p_4 + \alpha_{82}p_1p_4 = 0 \quad (69)$$

$$\ddot{q}_4 + \alpha_{86}p_2^2 + \alpha_{87}p_4 + \alpha_{87}q_4 + \alpha_{75}\dot{q}_4 + \alpha_{84}p_{s3}p_1 + \alpha_{85}p_{s2}p_2 + \alpha_{84}p_{s1}p_3 + \alpha_{84}p_1p_3 = 0 \quad (70)$$

$$\begin{aligned} &\alpha_{88}p_{s1} + \alpha_{89}p_1 + \alpha_{11}\dot{p}_1 + \alpha_{106}\dot{q}_1 + \alpha_{107}\dot{V}_{AC} + \alpha_{90}p_{s1}^2\dot{p}_1 \\ &+ \alpha_{91}p_{s2}\dot{p}_1 + \alpha_{14}p_{s2}^2\dot{p}_1 + \alpha_{18}p_{s3}^2\dot{p}_1 + \alpha_{22}p_{s4}^2\dot{p}_1 \\ &+ \alpha_{93}q_{s2}\dot{p}_1 + \alpha_{90}p_1^2\dot{p}_1 + \alpha_{91}p_2\dot{p}_1 + \alpha_{14}p_2^2\dot{p}_1 \\ &+ \alpha_{18}p_3^2\dot{p}_1 + \alpha_{22}p_4^2\dot{p}_1 + \alpha_{93}q_2\dot{p}_1 + \alpha_{91}p_{s1}\dot{p}_2 \\ &+ \alpha_{98}p_{s3}\dot{p}_2 + \alpha_{100}q_{s1}\dot{p}_2 + \alpha_{101}q_{s3}\dot{p}_2 + \alpha_{91}p_1\dot{p}_2 \\ &+ \alpha_{98}p_3\dot{p}_2 + \alpha_{100}q_1\dot{p}_2 + \alpha_{101}q_3\dot{p}_2 + \alpha_{15}p_{s1}^2\dot{p}_3 \\ &+ \alpha_{98}p_{s2}\dot{p}_3 + \alpha_{17}p_{s2}^2\dot{p}_3 + \alpha_{102}p_{s4}\dot{p}_3 + \alpha_{103}q_{s2}\dot{p}_3 \\ &+ \alpha_{104}q_{s4}\dot{p}_3 + \alpha_{15}p_1^2\dot{p}_3 + \alpha_{98}p_2\dot{p}_3 + \alpha_{17}p_2^2\dot{p}_3 \\ &+ \alpha_{102}p_4\dot{p}_3 + \alpha_{103}q_2\dot{p}_3 + \alpha_{104}q_4\dot{p}_3 + \alpha_{102}p_{s3}\dot{p}_4 \\ &+ \alpha_{105}q_{s3}\dot{p}_4 + \alpha_{102}p_3\dot{p}_4 + \alpha_{105}q_3\dot{p}_4 + \alpha_{100}p_{s2}\dot{q}_1 \\ &+ \alpha_{100}p_2\dot{q}_1 + \alpha_{93}p_{s1}\dot{q}_2 + \alpha_{103}p_{s3}\dot{q}_2 + \alpha_{93}p_1\dot{q}_2 \\ &+ \alpha_{103}p_3\dot{q}_2 + \alpha_{101}p_{s2}\dot{q}_3 + \alpha_{105}p_{s4}\dot{q}_3 + \alpha_{101}p_2\dot{q}_3 \\ &+ \alpha_{105}p_4\dot{q}_3 + \alpha_{104}p_{s3}\dot{q}_4 + \alpha_{104}p_3\dot{q}_4 + \alpha_{92}p_{s1}p_{s3}\dot{p}_1 \\ &+ \alpha_{19}p_{s2}p_{s4}\dot{p}_1 + \alpha_{94}p_{s1}p_1\dot{p}_1 + \alpha_{92}p_{s3}p_1\dot{p}_1 \\ &+ \alpha_{95}p_{s2}p_2\dot{p}_1 + \alpha_{19}p_{s4}p_2\dot{p}_1 + \alpha_{92}p_{s1}p_3\dot{p}_1 \\ &+ \alpha_{96}p_{s3}p_3\dot{p}_1 + \alpha_{92}p_1p_3\dot{p}_1 + \alpha_{19}p_{s2}p_4\dot{p}_1 \\ &+ \alpha_{97}p_{s4}p_4\dot{p}_1 + \alpha_{19}p_2p_4\dot{p}_1 + \alpha_{95}p_{s1}p_{s2}\dot{p}_2 \\ &+ \alpha_{99}p_{s2}p_{s3}\dot{p}_2 + \alpha_{19}p_{s1}p_{s4}\dot{p}_2 + \alpha_{21}p_{s3}p_{s4}\dot{p}_2 \\ &+ \alpha_{95}p_{s2}p_1\dot{p}_2 + \alpha_{19}p_{s4}p_1\dot{p}_2 + \alpha_{95}p_{s1}p_2\dot{p}_2 \\ &+ \alpha_{99}p_{s3}p_2\dot{p}_2 + \alpha_{95}p_1p_2\dot{p}_2 + \alpha_{99}p_{s2}p_3\dot{p}_2 \\ &+ \alpha_{21}p_{s4}p_3\dot{p}_2 + \alpha_{99}p_2p_3\dot{p}_2 + \alpha_{19}p_{s1}p_4\dot{p}_2 \\ &+ \alpha_{21}p_{s3}p_4\dot{p}_2 + \alpha_{19}p_1p_4\dot{p}_2 + \alpha_{21}p_3p_4\dot{p}_2 \\ &+ \alpha_{96}p_{s1}p_{s3}\dot{p}_3 + \alpha_{21}p_{s2}p_{s4}\dot{p}_3 + \alpha_{92}p_{s1}p_1\dot{p}_3 \\ &+ \alpha_{96}p_{s3}p_1\dot{p}_3 + \alpha_{99}p_{s2}p_2\dot{p}_3 + \alpha_{21}p_{s4}p_2\dot{p}_3 \\ &+ \alpha_{96}p_{s1}p_3\dot{p}_3 + \alpha_{96}p_1p_3\dot{p}_3 + \alpha_{21}p_{s2}p_4\dot{p}_3 \\ &+ \alpha_{21}p_2p_4\dot{p}_3 + \alpha_{19}p_{s1}p_{s2}\dot{p}_4 + \alpha_{21}p_{s2}p_{s3}\dot{p}_4 \\ &+ \alpha_{97}p_{s1}p_{s4}\dot{p}_4 + \alpha_{19}p_{s2}p_1\dot{p}_4 + \alpha_{97}p_{s4}p_1\dot{p}_4 \\ &+ \alpha_{19}p_{s1}p_2\dot{p}_4 + \alpha_{21}p_{s3}p_2\dot{p}_4 + \alpha_{19}p_1p_2\dot{p}_4 \\ &+ \alpha_{21}p_{s2}p_3\dot{p}_4 + \alpha_{21}p_2p_3\dot{p}_4 + \alpha_{97}p_{s1}p_4\dot{p}_4 \\ &+ \alpha_{97}p_1p_4\dot{p}_4 = 0 \end{aligned} \quad (71)$$

$$\begin{aligned} &\alpha_{88}p_{s2} + \alpha_{89}p_2 + \alpha_{11}\dot{p}_2 + \alpha_{106}\dot{q}_2 + \alpha_{108}p_{s1}\dot{p}_1 + \alpha_{110}p_{s3}\dot{p}_1 \\ &+ \alpha_{112}q_{s1}\dot{p}_1 + \alpha_{113}q_{s3}\dot{p}_1 + \alpha_{108}p_1\dot{p}_1 + \alpha_{110}p_3\dot{p}_1 \\ &+ \alpha_{112}q_1\dot{p}_1 + \alpha_{113}q_3\dot{p}_1 + \alpha_{31}p_{s1}^2\dot{p}_2 + \alpha_{114}p_{s2}^2\dot{p}_2 \\ &+ \alpha_{35}p_{s3}^2\dot{p}_2 + \alpha_{115}p_{s4}\dot{p}_2 + \alpha_{40}p_{s4}^2\dot{p}_2 + \alpha_{116}q_{s4}\dot{p}_2 \\ &+ \alpha_{31}p_1^2\dot{p}_2 + \alpha_{114}p_2^2\dot{p}_2 + \alpha_{35}p_3^2\dot{p}_2 + \alpha_{115}p_4\dot{p}_2 \\ &+ \alpha_{40}p_4^2\dot{p}_2 + \alpha_{116}q_4\dot{p}_2 + \alpha_{110}p_{s1}\dot{p}_3 + \alpha_{121}q_{s1}\dot{p}_3 \\ &+ \alpha_{110}p_1\dot{p}_3 + \alpha_{121}q_1\dot{p}_3 + \alpha_{36}p_{s1}^2\dot{p}_4 + \alpha_{115}p_{s2}\dot{p}_4 \\ &+ \alpha_{39}p_{s3}^2\dot{p}_4 + \alpha_{122}q_{s2}\dot{p}_4 + \alpha_{36}p_1^2\dot{p}_4 + \alpha_{115}p_2\dot{p}_4 \end{aligned}$$



$$\begin{aligned} &+ \alpha_{39}p_3^2\dot{p}_4 + \alpha_{122}q_2\dot{p}_4 + \alpha_{112}p_{s1}\dot{q}_1 + \alpha_{121}p_{s3}\dot{q}_1 \\ &+ \alpha_{112}p_1\dot{q}_1 + \alpha_{121}p_3\dot{q}_1 + \alpha_{122}p_{s4}\dot{q}_2 + \alpha_{122}p_4\dot{q}_2 \\ &+ \alpha_{113}p_{s1}\dot{q}_3 + \alpha_{113}p_1\dot{q}_3 + \alpha_{116}p_{s2}\dot{q}_4 + \alpha_{116}p_2\dot{q}_4 \\ &+ \alpha_{109}p_{s1}p_{s2}\dot{p}_1 + \alpha_{34}p_{s2}p_{s3}\dot{p}_1 + \alpha_{111}p_{s1}p_{s4}\dot{p}_1 \\ &+ \alpha_{38}p_{s3}p_{s4}\dot{p}_1 + \alpha_{109}p_{s2}p_1\dot{p}_1 + \alpha_{111}p_{s4}p_1\dot{p}_1 \\ &+ \alpha_{109}p_{s1}p_2\dot{p}_1 + \alpha_{34}p_{s3}p_2\dot{p}_1 + \alpha_{109}p_1p_2\dot{p}_1 \\ &+ \alpha_{34}p_{s2}p_3\dot{p}_1 + \alpha_{38}p_{s4}p_3\dot{p}_1 + \alpha_{34}p_2p_3\dot{p}_1 \\ &+ \alpha_{111}p_{s1}p_4\dot{p}_1 + \alpha_{38}p_{s3}p_4\dot{p}_1 + \alpha_{111}p_1p_4\dot{p}_1 \\ &+ \alpha_{38}p_3p_4\dot{p}_1 + \alpha_{34}p_{s1}p_{s3}\dot{p}_2 + \alpha_{109}p_{s1}p_1\dot{p}_2 \\ &+ \alpha_{34}p_{s3}p_1\dot{p}_2 + \alpha_{117}p_{s2}p_2\dot{p}_2 + \alpha_{34}p_{s1}p_3\dot{p}_2 \\ &+ \alpha_{118}p_{s3}p_3\dot{p}_2 + \alpha_{34}p_1p_3\dot{p}_2 + \alpha_{119}p_{s4}p_4\dot{p}_2 \\ &+ \alpha_{34}p_{s1}p_{s2}\dot{p}_3 + \alpha_{118}p_{s2}p_{s3}\dot{p}_3 + \alpha_{38}p_{s1}p_{s4}\dot{p}_3 \\ &+ \alpha_{120}p_{s3}p_{s4}\dot{p}_3 + \alpha_{34}p_{s2}p_1\dot{p}_3 + \alpha_{38}p_{s4}p_1\dot{p}_3 \\ &+ \alpha_{34}p_{s1}p_2\dot{p}_3 + \alpha_{118}p_{s3}p_2\dot{p}_3 + \alpha_{34}p_1p_2\dot{p}_3 \\ &+ \alpha_{118}p_{s2}p_3\dot{p}_3 + \alpha_{120}p_{s4}p_3\dot{p}_3 + \alpha_{118}p_2p_3\dot{p}_3 \\ &+ \alpha_{38}p_{s1}p_4\dot{p}_3 + \alpha_{120}p_{s3}p_4\dot{p}_3 + \alpha_{38}p_1p_4\dot{p}_3 \\ &+ \alpha_{120}p_3p_4\dot{p}_3 + \alpha_{38}p_{s1}p_{s3}\dot{p}_4 + \alpha_{119}p_{s2}p_{s4}\dot{p}_4 \\ &+ \alpha_{111}p_{s1}p_1\dot{p}_4 + \alpha_{38}p_{s3}p_1\dot{p}_4 + \alpha_{119}p_{s4}p_2\dot{p}_4 \\ &+ \alpha_{38}p_{s1}p_3\dot{p}_4 + \alpha_{120}p_{s3}p_3\dot{p}_4 + \alpha_{38}p_1p_3\dot{p}_4 \\ &+ \alpha_{119}p_{s2}p_4\dot{p}_4 + \alpha_{119}p_2p_4\dot{p}_4 = 0 \end{aligned} \quad (72)$$

$$\begin{aligned} &\alpha_{88}p_{s3} + \alpha_{89}p_3 + \alpha_{11}\dot{p}_3 + \alpha_{106}\dot{q}_3 + \alpha_{136}\dot{V}_{AC} + \alpha_{123}p_{s1}^2\dot{p}_1 \\ &+ \alpha_{124}p_{s2}\dot{p}_1 + \alpha_{48}p_{s2}^2\dot{p}_1 + \alpha_{126}p_{s4}\dot{p}_1 + \alpha_{127}q_{s2}\dot{p}_1 \\ &+ \alpha_{128}q_{s4}\dot{p}_1 + \alpha_{123}p_1^2\dot{p}_1 + \alpha_{124}p_2\dot{p}_1 + \alpha_{48}p_2^2\dot{p}_1 \\ &+ \alpha_{126}p_4\dot{p}_1 + \alpha_{127}q_2\dot{p}_1 + \alpha_{128}q_4\dot{p}_1 + \alpha_{124}p_{s1}\dot{p}_2 \\ &+ \alpha_{127}q_{s1}\dot{p}_2 + \alpha_{124}p_1\dot{p}_2 + \alpha_{127}q_1\dot{p}_2 + \alpha_{49}p_{s1}^2\dot{p}_3 \\ &+ \alpha_{50}p_{s2}^2\dot{p}_3 + \alpha_{132}p_{s3}^2\dot{p}_3 + \alpha_{55}p_{s4}^2\dot{p}_3 + \alpha_{49}p_1^2\dot{p}_3 \\ &+ \alpha_{50}p_2^2\dot{p}_3 + \alpha_{132}p_3^2\dot{p}_3 + \alpha_{55}p_4^2\dot{p}_3 + \alpha_{126}p_{s1}\dot{p}_4 \\ &+ \alpha_{135}q_{s1}\dot{p}_4 + \alpha_{126}p_1\dot{p}_4 + \alpha_{135}q_1\dot{p}_4 + \alpha_{127}p_{s2}\dot{q}_1 \\ &+ \alpha_{135}p_{s4}\dot{q}_1 + \alpha_{127}p_2\dot{q}_1 + \alpha_{135}p_4\dot{q}_1 + \alpha_{127}p_{s1}\dot{q}_2 \\ &+ \alpha_{127}p_1\dot{q}_2 + \alpha_{128}p_{s1}\dot{q}_4 + \alpha_{128}p_1\dot{q}_4 + \alpha_{125}p_{s1}p_{s3}\dot{p}_1 \\ &+ \alpha_{53}p_{s2}p_{s4}\dot{p}_1 + \alpha_{129}p_{s1}p_1\dot{p}_1 + \alpha_{125}p_{s3}p_1\dot{p}_1 \\ &+ \alpha_{130}p_{s2}p_2\dot{p}_1 + \alpha_{53}p_{s4}p_2\dot{p}_1 + \alpha_{125}p_{s1}p_3\dot{p}_1 \\ &+ \alpha_{125}p_1p_3\dot{p}_1 + \alpha_{53}p_{s2}p_4\dot{p}_1 + \alpha_{53}p_2p_4\dot{p}_1 \\ &+ \alpha_{130}p_{s1}p_{s2}\dot{p}_2 + \alpha_{131}p_{s2}p_{s3}\dot{p}_2 + \alpha_{53}p_{s1}p_{s4}\dot{p}_2 \\ &+ \alpha_{54}p_{s3}p_{s4}\dot{p}_2 + \alpha_{130}p_{s2}p_1\dot{p}_2 + \alpha_{53}p_{s4}p_1\dot{p}_2 \\ &+ \alpha_{130}p_{s1}p_2\dot{p}_2 + \alpha_{131}p_{s3}p_2\dot{p}_2 + \alpha_{130}p_1p_2\dot{p}_2 \\ &+ \alpha_{131}p_{s2}p_3\dot{p}_2 + \alpha_{54}p_{s4}p_3\dot{p}_2 + \alpha_{131}p_2p_3\dot{p}_2 \\ &+ \alpha_{53}p_{s1}p_4\dot{p}_2 + \alpha_{54}p_{s3}p_4\dot{p}_2 + \alpha_{53}p_1p_4\dot{p}_2 \\ &+ \alpha_{54}p_3p_4\dot{p}_2 + \alpha_{54}p_{s2}p_{s4}\dot{p}_3 + \alpha_{125}p_{s1}p_1\dot{p}_3 \\ &+ \alpha_{131}p_{s2}p_2\dot{p}_3 + \alpha_{54}p_{s4}p_2\dot{p}_3 + \alpha_{133}p_{s3}p_3\dot{p}_3 \\ &+ \alpha_{54}p_{s2}p_4\dot{p}_3 + \alpha_{134}p_{s4}p_4\dot{p}_3 + \alpha_{54}p_2p_4\dot{p}_3 \\ &+ \alpha_{53}p_{s1}p_{s2}\dot{p}_4 + \alpha_{54}p_{s2}p_{s3}\dot{p}_4 + \alpha_{134}p_{s3}p_{s4}\dot{p}_4 \\ &+ \alpha_{53}p_{s2}p_1\dot{p}_4 + \alpha_{53}p_{s1}p_2\dot{p}_4 + \alpha_{54}p_{s3}p_2\dot{p}_4 \\ &+ \alpha_{53}p_1p_2\dot{p}_4 + \alpha_{54}p_{s2}p_3\dot{p}_4 + \alpha_{134}p_{s4}p_3\dot{p}_4 \\ &+ \alpha_{54}p_2p_3\dot{p}_4 + \alpha_{134}p_{s3}p_4\dot{p}_4 + \alpha_{134}p_3p_4\dot{p}_4 = 0 \end{aligned} \quad (73)$$

$$\begin{aligned}
 &\alpha_{88}p_{s4} + \alpha_{89}p_4 + \alpha_{11}\dot{p}_4 + \alpha_{106}\dot{q}_4 + \alpha_{138}p_{s3}\dot{p}_1 + \alpha_{140}q_{s3}\dot{p}_1 \\
 &+ \alpha_{138}p_3\dot{p}_1 + \alpha_{140}q_3\dot{p}_1 + \alpha_{141}p_{s1}^2\dot{p}_2 + \alpha_{142}p_{s2}\dot{p}_2 \\
 &+ \alpha_{64}p_{s3}^2\dot{p}_2 + \alpha_{144}q_{s2}\dot{p}_2 + \alpha_{141}p_1^2\dot{p}_2 + \alpha_{142}p_2\dot{p}_2 \\
 &+ \alpha_{64}p_3^2\dot{p}_2 + \alpha_{144}q_2\dot{p}_2 + \alpha_{138}p_{s1}\dot{p}_3 + \alpha_{140}q_{s1}\dot{p}_3 \\
 &+ \alpha_{138}p_1\dot{p}_3 + \alpha_{140}q_1\dot{p}_3 + \alpha_{65}p_{s1}^2\dot{p}_4 + \alpha_{66}p_{s2}^2\dot{p}_4 \\
 &+ \alpha_{67}p_{s3}^2\dot{p}_4 + \alpha_{147}p_{s4}^2\dot{p}_4 + \alpha_{65}p_1^2\dot{p}_4 + \alpha_{66}p_2^2\dot{p}_4 \\
 &+ \alpha_{67}p_3^2\dot{p}_4 + \alpha_{147}p_4^2\dot{p}_4 + \alpha_{140}p_{s3}\dot{q}_1 + \alpha_{140}p_3\dot{q}_1 \\
 &+ \alpha_{144}p_{s2}\dot{q}_2 + \alpha_{144}p_2\dot{q}_2 + \alpha_{140}p_{s1}\dot{q}_3 + \alpha_{140}p_1\dot{q}_3 \\
 &+ \alpha_{137}p_{s1}p_{s2}\dot{p}_1 + \alpha_{63}p_{s2}p_{s3}\dot{p}_1 + \alpha_{139}p_{s1}p_{s4}\dot{p}_1 \\
 &+ \alpha_{137}p_{s2}p_1\dot{p}_1 + \alpha_{139}p_{s4}p_1\dot{p}_1 + \alpha_{137}p_{s1}p_2\dot{p}_1 \\
 &+ \alpha_{63}p_{s3}p_2\dot{p}_1 + \alpha_{137}p_1p_2\dot{p}_1 + \alpha_{63}p_{s2}p_3\dot{p}_1 \\
 &+ \alpha_{63}p_2p_3\dot{p}_1 + \alpha_{139}p_{s1}p_4\dot{p}_1 + \alpha_{139}p_1p_4\dot{p}_1 \\
 &+ \alpha_{63}p_{s1}p_{s3}\dot{p}_2 + \alpha_{143}p_{s2}p_{s4}\dot{p}_2 + \alpha_{137}p_{s1}p_1\dot{p}_2 \\
 &+ \alpha_{63}p_{s3}p_1\dot{p}_2 + \alpha_{143}p_{s4}p_2\dot{p}_2 + \alpha_{63}p_{s1}p_3\dot{p}_2 \\
 &+ \alpha_{145}p_{s3}p_3\dot{p}_2 + \alpha_{63}p_1p_3\dot{p}_2 + \alpha_{143}p_{s2}p_4\dot{p}_2 \\
 &+ \alpha_{143}p_2p_4\dot{p}_2 + \alpha_{63}p_{s1}p_{s2}\dot{p}_3 + \alpha_{145}p_{s2}p_{s3}\dot{p}_3 \\
 &+ \alpha_{146}p_{s3}p_{s4}\dot{p}_3 + \alpha_{63}p_{s2}p_1\dot{p}_3 + \alpha_{63}p_{s1}p_2\dot{p}_3 \\
 &+ \alpha_{145}p_{s3}p_2\dot{p}_3 + \alpha_{63}p_1p_2\dot{p}_3 + \alpha_{145}p_{s2}p_3\dot{p}_3 \\
 &+ \alpha_{146}p_{s4}p_3\dot{p}_3 + \alpha_{145}p_2p_3\dot{p}_3 + \alpha_{146}p_{s3}p_4\dot{p}_3 \\
 &+ \alpha_{146}p_3p_4\dot{p}_3 + \alpha_{139}p_{s1}p_1\dot{p}_4 + \alpha_{143}p_{s2}p_2\dot{p}_4 \\
 &+ \alpha_{146}p_{s3}p_3\dot{p}_4 + \alpha_{148}p_{s4}p_4\dot{p}_4 = 0 \tag{74}
 \end{aligned}$$

where the coefficients α_i depend on the substrate properties and the permittivity ratio r .

ORCID iDs

Alaa Elhady  <https://orcid.org/0000-0002-6963-8462>
 Eihab Abdel-Rahman  <https://orcid.org/0000-0002-3709-7593>

References

[1] Ellison W, Balana A, Delbos G, Lamkaouchi K, Eymard L, Guillou C and Prigent C 1998 New permittivity measurements of seawater *Radio Sci.* **33** 639–48
 [2] Meissner T and Wentz F J 2004 The complex dielectric constant of pure and sea water from microwave satellite observations *IEEE Trans. Geosci. Remote Sens.* **42** 1836–49
 [3] Robert Birchak J, Gerald Gardner C, Hipp J E and Victor J M 1974 High dielectric constant microwave probes for sensing soil moisture *Proc. IEEE* **62** 93–98
 [4] Brock K and Stoakes D 1973 Oil permittivity sensor *US Patent* 3,746,974
 [5] Folgero K, Friiso T, Hilland J and Tjomsland T 1995 A broad-band and high-sensitivity dielectric spectroscopy measurement system for quality determination of low-permittivity fluids *Meas. Sci. Technol.* **6** 995
 [6] Grant E H, McClean V E R, Nightingale N R V, Sheppard R J and Chapman M J 1986 Dielectric behavior of water in biological solutions: studies on myoglobin, human low-density lipoprotein and polyvinylpyrrolidone *Bioelectromagnetics* **7** 151–62
 [7] Jamal F I, Guha S, Eissa M H, Borngräber J, Meliani C, Ng H J, Kissinger D and Wessel J 2017 Low-power

miniature k -band sensors for dielectric characterization of biomaterials *IEEE Trans. Microw. Theory Tech.* **65** 1012–23
 [8] Chen T, Dubuc D, Poupot M, Fournie J-J and Grenier K 2012 Accurate nanoliter liquid characterization up to 40 GHz for biomedical applications: toward noninvasive living cells monitoring *IEEE Trans. Microw. Theory Tech.* **60** 4171–7
 [9] Hofmann M, Fischer G, Weigel R and Kissinger D 2013 Microwave-based noninvasive concentration measurements for biomedical applications *IEEE Trans. Microw. Theory Tech.* **61** 2195–204
 [10] Taeb A, Basha M A, Gigoyan S, Marsden M and Safavi-Naeini S 2013 Label-free DNA sensing using millimeter-wave silicon WGM resonator *Opt. Express* **21** 19467–72
 [11] Khan U, Al-Moayed N, Nguyen N, Obol M, Korolev K, Afsar M and Naber S 2007 High frequency dielectric characteristics of tumorous and non-tumorous breast tissues *Microwave Symp. 2007 IEEE/MTT-S Int.* (IEEE) pp 1341–4
 [12] Qiao G, Wang W, Duan W, Zheng F, Sinclair A J and Chatwin C R 2012 Bioimpedance analysis for the characterization of breast cancer cells in suspension *IEEE Trans. Biomed. Eng.* **59** 2321–9
 [13] Van Der Touw F, Briede J W H and Mandel M 1973 Electric permittivity of alfalfa mosaic virus in aqueous solutions *Biopolymers* **12** 111–9
 [14] Hughes M P, Morgan H and Rixon F J 2002 Measuring the dielectric properties of herpes simplex virus type 1 virions with dielectrophoresis *Biochim. Biophys. Acta* **1571** 1–8
 [15] Muñoz-Enano J, Martel J, Vélez P, Medina F, Su L and Martín F 2021 Parametric analysis of the edge capacitance of uniform slots and application to frequency-variation permittivity sensors *Appl. Sci.* **11** 7000
 [16] Ellis C D, Davidson J L and Baginski T A 1989 Microelectronic moisture sensor from variable dielectric capacitances of polyimide film *Proc., 8th University/Government/Industry Microelectronics Symp.* (IEEE) pp 87–91
 [17] Risos A, Long N, Hunze A and Gouws G 2017 Interdigitated sensors: a design principle for accurately measuring the permittivity of industrial oils *IEEE Sens. J.* **17** 6232–9
 [18] Alu A and Engheta N 2008 Dielectric sensing in ϵ -near-zero narrow waveguide channels *Phys. Rev. B* **78** 045102
 [19] Lobato-Morales H, Corona-Chávez A, Olvera-Cervantes J L, Chávez-Pérez R A and Medina-Monroy J L 2014 Wireless sensing of complex dielectric permittivity of liquids based on the RFID *IEEE Trans. Microw. Theory Tech.* **62** 2160–7
 [20] Wiltshire B D, Zarifi T and Zarifi M H 2019 Passive split ring resonator tag configuration for RFID-based wireless permittivity sensing *IEEE Sens. J.* **20** 1904–11
 [21] Karami M, Rezaei P, Kiani S and Sadeghzadeh R A 2017 Modified planar sensor for measuring dielectric constant of liquid materials *Electron. Lett.* **53** 1300–2
 [22] Ebrahimi A, Scott J and Ghorbani K 2019 Ultrahigh-sensitivity microwave sensor for microfluidic complex permittivity measurement *IEEE Trans. Microw. Theory Tech.* **67** 4269–77
 [23] Turgul V and Kale I 2016 Characterization of the complex permittivity of glucose/water solutions for noninvasive RF/microwave blood glucose sensing *2016 IEEE Int. Instrumentation and Measurement Technology Conf. Proc.* (IEEE) pp 1–5
 [24] Kiani S, Rezaei P and Navaei M 2020 Dual-sensing and dual-frequency microwave SRR sensor for liquid samples permittivity detection *Measurement* **160** 107805
 [25] Chuma E L, Iano Y, Fontgalland G, Roger L L B and Loschi H 2020 PCB-integrated non-destructive microwave sensor for liquid dielectric spectroscopy based on planar metamaterial resonator *Sens. Actuators A* **312** 112112

- [26] Su L, Mata-Contreras J, Vélez P, Fernández-Prieto A and Martín F 2018 Analytical method to estimate the complex permittivity of oil samples *Sensors* **18** 984
- [27] Withayachumankul W, Jaruwongrunsee K, Tuantranont A, Fumeaux C and Abbott D 2013 Metamaterial-based microfluidic sensor for dielectric characterization *Sens. Actuators A* **189** 233–7
- [28] Fratticcioli E, Dionigi M and Sorrentino R 2004 A simple and low-cost measurement system for the complex permittivity characterization of materials *IEEE Trans. Instrum. Meas.* **53** 1071–7
- [29] Chen S, Zhou F, Xu K, Zhao P, Yang Y, Zhu Xi and Wang G 2020 A portable microwave interferometry sensor for permittivity detection based on CCMRC *IEEE Access* **8** 140323–32
- [30] Costa F, Gentile A, Genovesi S, Buoncristiani L, Lazaro A, Villarino R and Girbau D 2018 A depolarizing chipless RF label for dielectric permittivity sensing *IEEE Microw. Wirel. Compon. Lett.* **28** 371–3
- [31] Nelson S O *et al* 1995 Assessment of microwave permittivity for sensing peach maturity *Trans. ASAE* **38** 579–85
- [32] Bajestan M M, Helmy A A, Hedayati H and Entesari K 2014 A 0.62–10 GHz complex dielectric spectroscopy system in CMOS *IEEE Trans. Microw. Theory Tech.* **62** 3522–37
- [33] Chretiennot T, Dubuc D and Grenier K 2012 A microwave and microfluidic planar resonator for efficient and accurate complex permittivity characterization of aqueous solutions *IEEE Trans. Microw. Theory Tech.* **61** 972–8
- [34] Laemmle B, Schmalz K, Scheytt J C, Weigel R and Kissinger D 2013 A 125-GHz permittivity sensor with read-out circuit in a 250-nm SiGe BiCMOS technology *IEEE Trans. Microw. Theory Tech.* **61** 2185–94
- [35] Elhadidy O, Shakib S, Krenek K, Palermo S and Entesari K 2015 A wide-band fully-integrated CMOS ring-oscillator PLL-based complex dielectric spectroscopy system *IEEE Trans. Circuits Syst. I* **62** 1940–9
- [36] Vlachogiannakis G, Hu Z, Shivamurthy H T, Neto A, Pertijs M A P, De Vreede L C N and Spirito M 2018 Miniaturized broadband microwave permittivity sensing for biomedical applications *IEEE J. Electromagn. RF Microw. Med. Biol.* **3** 48–55
- [37] Elhadidy O, Elkholy M, Helmy A A, Palermo S and Entesari K 2013 A CMOS fractional- n PLL-based microwave chemical sensor with 1.5% permittivity accuracy *IEEE Trans. Microw. Theory Tech.* **61** 3402–16
- [38] Islam M, Jagan Mohan Rao S, Kumar G, Pal B P and Chowdhury D R 2017 Role of resonance modes on terahertz metamaterials based thin film sensors *Sci. Rep.* **7** 7355
- [39] Bhardwaj A, Pratap D, Srivastava K V and Anantha Ramakrishna S 2021 Highly sensitive permittivity sensor using an inhomogeneous metamaterial cylindrical waveguide *IEEE Sens. J.* **21** 9120–7
- [40] Bleustein J L 1968 A new surface wave in piezoelectric materials *Appl. Phys. Lett.* **13** 412–3
- [41] Gulyaev Y V 1969 Electroacoustic surface waves in solids *ZhETF Pisma Redaktsiiu* **9** 63
- [42] El Baroudi A and Le Pommellec J Y 2021 Bleustein–Gulyaev waves in a finite piezoelectric material loaded with a viscoelastic fluid *Wave Motion* **101** 102695
- [43] Guo F L and Sun R 2008 Propagation of Bleustein–Gulyaev wave in 6 mm piezoelectric materials loaded with viscous liquid *Int. J. Solids Struct.* **45** 3699–710
- [44] Guo F L, Wang G Q and Rogerson G A 2012 Inverse determination of liquid viscosity by means of the Bleustein–Gulyaev wave *Int. J. Solids Struct.* **49** 2115–20
- [45] Kiełczyński P, Pajewski W, Szalewski M and Balcerzak A 2004 Measurement of the shear storage modulus and viscosity of liquids using the Bleustein–Gulyaev wave *Rev. Sci. Instrum.* **75** 2362–7
- [46] Zhang C, Caron J J and Vetelino J F 2001 The Bleustein–Gulyaev wave for liquid sensing applications *Sens. Actuators B* **76** 64–68
- [47] Alshaiikh F 2020 Electromechanical coupling of Bleustein–Gulyaev wave propagation in rotating prestressed piezoelectric layered materials *Contin. Mech. Thermodyn.* **32** 749–59
- [48] Fang H, Yang J and Jiang Q 1999 Gyroscopic effect on surface waves in piezoelectrics *1999 IEEE Ultrasonics Symp. Proc.* vol 1 (IEEE) pp 497–500
- [49] Morozumi K, Kadota M and Hayashi S 1996 Characteristics of BGS wave resonators using ceramic substrates and their applications *1996 IEEE Ultrasonics Symp. Proc.* vol 1 (IEEE) pp 81–86
- [50] Kadota M, Ago J, Horiuchi H and Morii H 2000 Transversely coupled resonator filters utilizing reflection of Bleustein–Gulyaev–Shimizu wave at free edges of substrate *Jpn. J. Appl. Phys.* **39** 3045
- [51] Kadota M, Ago J, Horiuchi H and Ikeura M 2002 Very small IF resonator filters using reflection of shear horizontal wave at free edges of substrate *IEEE Trans. Ultrason. Ferroelectr. Freq. Control* **49** 1269–79
- [52] Kadota M, Ago J, Horiuchi H and Ikeura M 2001 Longitudinally coupled resonator filter using edge reflection of Bleustein–Gulyaev–Shimizu and shear horizontal waves with various bandwidths realized by selecting substrates *Jpn. J. Appl. Phys.* **40** 3722
- [53] Kawasaki Z'ichro and Tanaka K 1978 Analysis of propagation characteristic of Bleustein–Gulyaev waves at surface imperfections *Appl. Phys. Lett.* **32** 83–85
- [54] Collet B, Destrade M and Maugin Gerard A 2006 Bleustein–Gulyaev waves in some functionally graded materials *Eur. J. Mech. A* **25** 695–706
- [55] Nakamura K 2007 Shear-horizontal piezoelectric surface acoustic waves *Jpn. J. Appl. Phys.* **46** 4421
- [56] Liu H, Kuang Z B and Cai Z M 2003 Propagation of Bleustein–Gulyaev waves in a prestressed layered piezoelectric structure *Ultrasonics* **41** 397–405
- [57] Liu Y, Ren K L, Hofmann H F and Zhang Q 2005 Investigation of electrostrictive polymers for energy harvesting *IEEE Trans. Ultrason. Ferroelectr. Freq. Control* **52** 2411–7
- [58] Elhady A, Basha M and Abdel-Rahman E M 2021 Analysis of tunable Bleustein–Gulyaev permittivity sensors *J. Appl. Phys.* **129** 164501
- [59] Ahmed A 2021 Tunable permittivity sensors *PhD Thesis* University of Waterloo, System Design Department, Waterloo, ON
- [60] Elhady A and Abdel-Rahman E M 2021 Characterization of shear horizontal waves using a 1D laser Doppler vibrometer *Sensors* **21** 2467
- [61] Younis M I 2011 *Mems Linear and Nonlinear Statics and Dynamics* vol 20 (Boston, MA: Springer Science & Business Media)
- [62] Meirovitch L 2001 *Fundamentals of Vibrations* (New York: McGraw-Hill)
- [63] Wolfram Research, Inc. Mathematica (available at: www.wolfram.com/mathematica) (Accessed 23 December 2020)
- [64] American piezo ceramics: properties of materials (available at: www.americanpiezo.com/apc-materials/piezoelectric-properties.html) (Accessed 23 December 2020)
- [65] Boston piezo optics (available at: www.bostonpiezooptics.com/lithium-niobate) (Accessed 5 June 2021)
- [66] Jiang S N, Jiang Q, Li X F, Guo S H, Zhou H G and Yang J S 2006 Piezoelectromagnetic waves in a ceramic plate between two ceramic half-spaces *Int. J. Solids Struct.* **43** 5799–810
- [67] Weis R S and Gaylord T K 1985 Lithium niobate: summary of physical properties and crystal structure *Appl. Phys. A* **37** 191–203

- [68] Jonscher A K 1977 The 'universal' dielectric response *Nature* **267** 673–9
- [69] Bhugra H and Piazza G 2017 *Piezoelectric MemS Resonators* (Berlin: Springer)
- [70] Rahman B M A and Haxha S 2002 Optimization of microwave properties for ultrahigh-speed etched and unetched lithium niobate electrooptic modulators *J. Lightwave Technol.* **20** 1856
- [71] Puranik S M, Kumbharkhane A C and Mehrotra S C 1993 Temperature dependent dielectric studies of ethanol and ethylene glycol using time domain reflectometry *Indian J. Phys. B* **67** 9–13
- [72] Kaatze U 1989 Complex permittivity of water as a function of frequency and temperature *J. Chem. Eng. Data* **34** 371–4
- [73] Elhady A, Basha M and Abdel-Rahman E M 2020 Tunable Bleustein–Gulyaev permittivity sensors *New Trends in Nonlinear Dynamics* (Berlin: Springer) pp 3–11
- [74] Caspers F 2012 RF engineering basic concepts: S-parameters *CERN Yellow Report CERN-2011-007* pp 67–78
- [75] Soluch W 2000 Scattering matrix approach to one-port SAW resonators *IEEE Trans. Ultrason. Ferroelectr. Freq. Control* **47** 1615–8
- [76] Kambali P N and Pandey A K 2015 Capacitance and force computation due to direct and fringing effects in MEMS/NEMS arrays *IEEE Sens. J.* **16** 375–82
- [77] DeAngelis D A and Schulze G W 2016 Performance of PZT8 versus PZT4 piezoceramic materials in ultrasonic transducers *Phys. Proc.* **87** 85–92
- [78] Gong S and Piazza G 2012 Laterally vibrating lithium niobate MEMS resonators with high electromechanical coupling and quality factor *2012 IEEE Int. Ultrasonics Symp.* (IEEE) pp 1051–4
- [79] Hu M and Duan F Li 2018 Design, fabrication and characterization of SAW devices on LiNbO₃ bulk and ZnO thin film substrates *Solid-State Electron.* **150** 28–34
- [80] Matsuda S, Miura M, Matsuda T, Ueda M, Satoh Y and Hashimoto K-Y 2011 Experimental studies of quality factor deterioration in shear-horizontal-type surface acoustic wave resonators caused by apodization of interdigital transducer *Jpn. J. Appl. Phys.* **50** 07HD14
- [81] Nakamura H, Yamada T, Igaki T, Nishimura K, Ishizaki T and Ogawa K 2000 A practical SPUDT design for saw filters with different-width split-finger interdigital transducers *2000 IEEE Ultrasonics Symp. Proc. Int. Symp. (Cat. No. 00CH37121)* vol 1 (IEEE) pp 105–8